

QATAR UNIVERSITY

COLLEGE OF ENGINEERING

DESIGN OF EMBEDDED 3D PRINTED SENSORS ON A ROBOT FOR MONITORING

AND CAPTURING ATMOSPHERIC CARBON DIOXIDE

BY

MOHAMMAD TALAL HOUKAN

A Thesis Submitted to

the College of Engineering

in Partial Fulfillment of the Requirements for the Degree of

Master of Science in Mechanical Engineering

January 2021

© 2021 Mohammad Talal Houkan. All Rights Reserved.

COMMITTEE PAGE

The members of the Committee approve the Thesis of
Mohammad Talal Houkan defended on 06/12/2020.

Dr. John-John Cabibihan
Thesis/Dissertation Supervisor

Dr. Kishor Kumar Sadasivuni
Co-Supervisor

Dr. Ho Seok Ahn
Committee Member

Dr. Jamil Renno
Committee Member

Approved:

Khalid Kamal Naji, Dean, College of Engineering

ABSTRACT

HOUKAN, MOHAMMAD T., Masters : January : 2021.;

Masters of Science in Mechanical Engineering

Title: Design of Embedded 3D Printed Sensors on a Robot for Monitoring and Capturing Atmospheric Carbon Dioxide

Supervisor of Thesis: John-John, Cabibihan.

Gas detection is a critical task in dangerous environments that involve hazardous or contaminant gases. Quick detection of gas leaks and their rectification ensure the protection of lives and safeguards equipment installed in workplaces and industrial sites. Extensive work has been done in remote monitoring of the gas leaks via sensors installed at the locations. Even though these devices can detect harmful gases in the environment, they are not designed to take instant action for gas/smoke removal. We have surveyed the literature and gathered information that smoke from the fire accidents causes a lack of visibility to the exit, and many untimely lives are lost. Thus, further research has to be carried out to develop devices that can not only detect the harmful gases but also have the technology for gas/smoke removal supported by standard protocols to mitigate the effects of the harmful gas on the surrounding environment, such as an explosion, asphyxiation, fire. This thesis addresses the tasks required for developing a mobile robot that not only detects the presence of leakage of harmful gas like carbon dioxide (CO₂), carbon monoxide (CO), ammonia NH₃, liquid petroleum gas (LPG) and broadcast the information via wireless communication modeling system but also has gas filtration mechanism that

helps in purifying the surrounding air that has been contaminated by the leakage of the harmful gas. The contributions presented in this thesis are three-fold. Firstly, the fabrication of gas sensors via a 3D printing technique. The 3D printing approach enables the bulk production of the sensors in a short period. It gives control over the repeatability, reproducibility, and sensitivity of the fabricated sensors, especially for CO₂.

DEDICATION

This thesis is dedicated to my parents.

ACKNOWLEDGMENTS

This thesis was supported by the NPRP grant # NPRP11S-1221-170116 from the Qatar National Research Fund (a member of Qatar Foundation). The statements made herein are solely the responsibility of the authors.

I am extremely grateful to Dr. Muni Raj Maurya and Dr. Karthik Kannan for their extensive help and support in preparing my thesis. I am also thankful to my supervisors Dr. Kishor Kumar and Dr. John-John for their help, advice, and mentorship.

TABLE OF CONTENTS

DEDICATION	v
ACKNOWLEDGMENTS	vi
LIST OF TABLES	x
LIST OF FIGURES	xi
Chapter 1: Introduction	1
Problem Statement	1
Aim and Objectives	1
Contribution and Scope	2
Content Organization	4
Chapter 2: literature review	6
CO2 Sensors	6
ROV with Adsorption Technology	8
3D Printing	9
CO2 Adsorption Materials	11
ROV Navigation	15
LIDAR	17
Kinect 360 Depth Camera	17
Robot Operating System	18

Characterization Techniques	18
X-Ray Diffraction.....	19
Scanning Electron Microscopy.....	22
Fourier-transform Infrared Spectroscopy	24
Current-Voltage Characteristics	25
Thermogravimetric Analysis	26
Chapter 3: materials and methods.....	28
Materials.....	28
Preparation of Nanomaterial (CNT/CuO) and Resin Nanocomposite (Resin/CNT/CuO)	28
3D Printing	29
Material Preparation for 3D Printing.....	29
3D Printing Process of CNT/CuO Nanocomposites.....	30
Gas Sensing Setup	35
Analysis.....	37
Gas Sensing	37
Instruments for Measuring Properties	37
Design of Filtration Pipe.....	38
Design of CO ₂ Capturing Process.....	38
Chapter 4: results and discussion.....	41

Introduction	41
Gas Sensing Properties of the 3D printed sensors.....	41
Characterization of the CNT/CuO/resin composite-based 3D printed CO2 sensor	41
Electrical Properties and Conductivity Measurements of the 3D Printed Sensor	43
Semiconductor Analysis	46
Sensitivity Analysis	47
FTIR.....	48
X-Ray Diffraction Patterns	48
Thermogravimetric Analysis Results	48
Robotic Vehicle Results	50
E-Nose	50
LiDAR Results	50
Depth Camera Results	52
Robot Vehicle Performance.....	52
CFD Analysis	55
Chapter 5: conclusion	58
References.....	59

LIST OF TABLES

Table 2.1 Different types of CO ₂ sensors and their sensitivities for specified conditions.....	7
Table 2.2. The following table shows the material and their relative properties for adsorption of CO ₂ in the literature	14
Table 4.1. Showing a table summarizing the simulation results.....	56

LIST OF FIGURES

Figure 1.1. Sensors, radars, camera, and adsorption materials work together to CO ₂ detection and removal	2
Figure 1.2. Flowchart showing the operation of the robot vehicle	3
Figure 2.1. Different types of 3D printing	12
Figure 2.2. Different types of CAD software used for preparing 3D models	12
Figure 2.3. Showing the core parts of Kinect [83]	18
Figure 2.4. (a) Electron scattering process. (b) Continuous X-ray spectrum at different target potential	20
Figure 2.5. (a) Process of characteristics X-ray. (b) Characteristics X-ray lines along a continuous spectrum	21
Figure 2.6. Schematic for Braggs law of diffraction	22
Figure 2.7. Schematic for SEM analysis. [84]	24
Figure 2.8. Schematic of energy dispersive X-ray setup	25
Figure 2.9. Block diagram of a FTIR spectrometer [85]	26
Figure 3.1. Schematic representation of SWCNT/CuO nanocomposite preparation via hydrothermal method	30
Figure 3.2. : Schematic showing the various challenges DLP based 3D printing of the sensors and modifications incorporated to overcome these limitations	32
Figure 3.3. Schematic representation of the synthesis of CNT/CuO/resin composite for DLP based 3D printing	32
Figure 3.4. Modifications in DLP 3D printer. (a) Designing a smaller printing tank. (b) Designing a smaller printing platform	33

Figure 3.5. The first four printed layers with light at exposure time of 80 sec	34
Figure 3.6. Delamination of the 3D printing object	35
Figure 3.7. 3D printed CNT(0.25 wt%)/CuO (1 wt%)/resin composite	36
Figure 3.8. Non-uniform printing of composite material	36
Figure 3.9. 3D printed array of sensor pads. (a) 3D design of the object. (b) 3D printed object	37
Figure 3.10. Photograph of gas sensor experimental set up	38
Figure 3.11. Showing the instruments used for characterization of the material	39
Figure 3.12. LCR meter used to obtain resistance values	40
Figure 3.13. Shows the designed hexagonal filter	40
Figure 3.14. The vehicle that used to clean the environmental CO ₂ and CO ₂ release from industries using renewable energy	41
Figure 4.1. SEM images of the 3D printed sensor	44
Figure 4.2. SEM images of the 3D printed sensor. (a) SEM image with calculated geometrical values in the horizontal direction. (b) SEM image with calculated geometrical values in the vertical direction	45
Figure 4.3. XRD plot of the 3D printed sensor. Inset shows the magnified image of the CuO peaks in the XRD plot	45
Figure 4.4. Shows continuous response of the composite 3d printed sensor to CO ₂ at different concentration	46
Figure 4.5. Schematic of the formation of conductive pathways in the polymer matrix according to percolation theory	47
Figure 4.6. Schematic diagram showing the percolation behavior in polymer/ conducting filler composites, point B onward (percolation threshold), point c onward	

(saturation level)	48
Figure 4.7. Showing the IV curve of the sensor	49
Figure 4.8. Figure shows a plot of the relative resistance vs CO2 concentration	50
Figure 4.9. X-ray diffraction analysis for pure resin and composite material	51
Figure 4.10. Showing TGA results of resin, filler, and composite	52
Figure 4.11. A sensor array is composed of different MOX sensors	53
Figure 4.12. Showing LiDAR image of Hallway	54
Figure 4.13. Showing a 3d map constructed from depth camera output [90]	55
Figure 4.14. Shows the Arduino code	57
Figure 4.15. Shows the python code connecting the Arduino	58
Figure 4.16. The overview of the robotic vehicle deployed for detection and capture of CO2	58
Figure 4.17. Flowchart showing simulation results for different twist angles	60
Figure 4.18. Showing surface increase with twist angle	61

Chapter 1: Introduction

In a fire emergency, many gases are emitted that are harmful to human health. Which acts as a hindrance against timely escape from the fire scene or could lead to serious chronic health problems. Most dangerous gases from such incidents that can cause asphyxiation or fatality in high dosage are smoke, carbon monoxide (CO), and carbon dioxide (CO₂). Smoke decreases sight in a situation where unobstructed vision and fast response are critical for survival. It contains particulates that are 2.5 microns, which are very hazardous to human health [1]. CO decreases the system's oxygen levels, causing headaches, reducing alertness, and angina, which is not optimal in a fire emergency since a clear mind is needed to escape. Traditionally, to solve gas leakage, a ventilation system is built to remove gases/smoke through vents in the building, and jet fans are installed in underground parking lots. However, this ventilation system may not exist in every building and is not meant to provide a solution for open areas containing toxic gas in high concentrations, such as large warehouses and assembly lines. Furthermore, the ventilation system may not be adequate, depending on the location of the fire. Hence, a more practical approach to deal with such gas leakage is necessary. This thesis proposes using a more localized solution where a robotic vehicle is tasked with the detection and capturing of CO₂.

1.1. Problem Statement

Despite the advancements in fire fighting techniques like filtration and ventilation systems in modern buildings and open spaces, the detection and removal of flammable and toxic gases remain a challenge. A rapid detection mechanism and immediate removal of gases are required to solve fires and fatalities due to gas leaks.

1.2. Aim and Objectives

To fabricate an embedded 3D printed sensor that works with built-in a capturing mechanism to remove CO₂/smoke and integrate that with a robotic vehicle. The aim can be achieved by meeting the following objectives:

- to design the 3d printing the sensor.
- fabricates the sensor.
- test and optimize the 3d printed sensor.
- integrates with a unit to remove of CO₂.
- fit to the robotic vehicle.

1.3. Contribution and Scope

To solve rapid gas leakage detection and elimination, we embedded 3D printed sensors for the detection of CO₂ and a complimentary CO₂ removal system onboard of a robotic vehicle. The mobile robot(ROV) will contain a filter for particulate matter (PM) and other filters to capture gases. The contains filters with high-speed fans to forcefully make a gas exchange with the outside air faster than regular diffusion. The filter will be fabricated using commercially available CO₂ absorbents employing foaming to allow the air to pass through for exchange. in Figure 1.2 A flowchart gives the pseudo-code of how the vehicle will operate. Figure 1.1 shows the various components of the proposed solution.

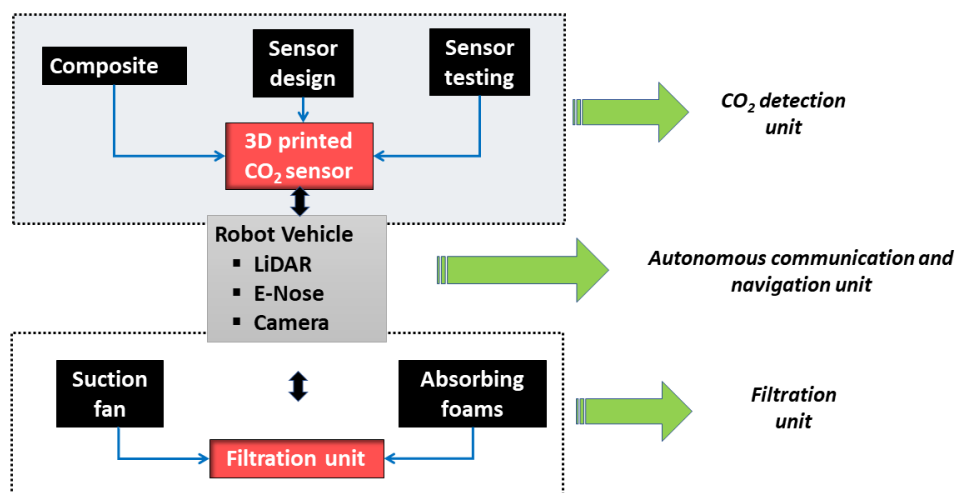
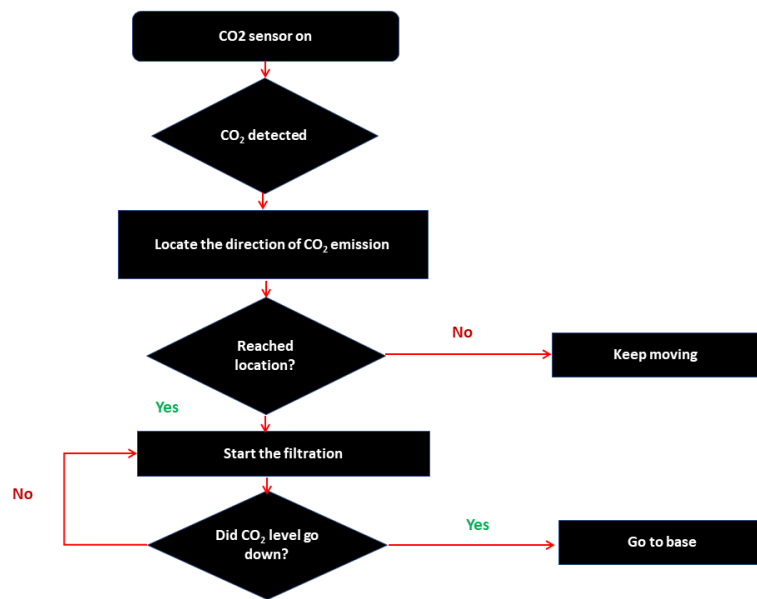


Figure 1.1. Sensors, radars, camera, and adsorption materials work together to CO₂ detection and removal.



11

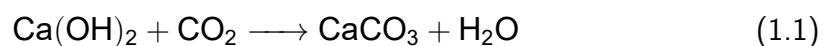
Figure 1.2. Flowchart showing the operation of the robot vehicle.

Inside the vehicle, few filters would take out the smoke PM and other emissions for capturing the CO/CO₂. The air pushed by the fan would be forced to go through a loop containing filters. The pressure drop due to the filters is studied using simulations, and other parameters related to capturing of gases are also optimized, for example, by increasing the distribution of air. Using results from computational fluid dynamics (CFD) analysis, the optimal loop configuration can be known. For CO₂ capture, optimizing the selectivity and effectiveness is essential, and commercially available materials have been tested for this application.

Recent advancements in sensors and sensing applications have achieved high-performance in real-time monitoring of physical changes in system states, toxic gas detection, diagnostics and fault detection, and continuous feedback. However, some of these sensors require advancements in sensitivity (true positive rate), specificity (true negative rate), and throughput (data transfer rate) with the instantaneous detection and notifications. Advances in additive manufacturing (also known as 3D printing) and embedded electronics have brought us closer to sensors with diverse working mechanisms, and 3D approaches open up a new frontier for sensor fabrication. 3D-printing

technology offers state-of-the-art fabrication methods for sensor fabrication and can create high-performance [2].

For 3D printing the sensors, we will take a resin (polymer) and mix it with conductive nanofillers. The mixture is 3D printed using the digital light processing (DLP) printing method to fabricate the CO₂ sensors. In the DLP method, the photo-polymerization of the mixture is carried out. To detect the gases, CO and CO₂, E-Nose made of 3D printed sensors is attached to the robot. Two other commercially available sensors are attached to the robot to detect the temperature and humidity. All the sensors are connected to the e-nose (electronic nose) of the robot. It acts as a compact device that enables the robot to sense the gases, temperature, and humidity as a standalone unit. An adsorption sponge is made of Ca(OH)₂ to adsorb CO₂ and CO in the air. The ROV contains solar cells and a rechargeable battery to power the fan attached to the adsorption system. The gases are fed to the adsorption system through the inlet fan attached to the system. The limestone reaction, a two-step reaction that converts calcium chloride to calcium carbonate, occurs in the adsorption sponge given by Eq. (1.1). The gas from the adsorption sponge is released into the atmosphere through the outlet fan attached to the adsorption system.



A Lidar (short for light detection and ranging) sensor is attached to the robot to navigate navigation. It can sense surrounding information within 10 meters of scanning radius. It works on the popular microcomputer Raspberry Pi mounted on the robot. Lidar works in both inside and outside areas (under sunlight), and it helps the robot avoid obstacles. The solar panel attached to this robot will help recharge the robot's battery while collecting the sensing data from different locations. We are focusing primarily on CO₂ detection and removal in this thesis. Other harmful gases could be detected and eliminated using a similar approach. However, they may require different adsorption materials, and the ROV design will need to be changed to accommodate those materials. However, they are not considered in this thesis.

1.4. Content Organization

Chapter 1 provided a brief introduction to the topic of CO₂ detection and removal from the atmosphere. It introduced our idea of an ROV that could be deployed to detect and remove CO₂. Chapter 2 opens with a comprehensive literature survey on CO₂ adsorption materials, CO₂ sensors, and some ROVs deployed for similar tasks. It provides background information on 3D printing, different sensing technologies used in the ROV such as depth camera, Lidar, and the modular robot operating system. Furthermore, it includes characterization techniques used for analyzing the surface properties of adsorption materials. Chapter 3 describes the methodology of the work. It includes the experiment setup, 3D printing technique used for printing the sensors, gas sensing setup, design of the robot vehicle, CO₂ capture by adsorption, and the material characterization using different techniques. Chapter 4 includes the results and discussion. It provides data and its interpretation from the various methodology stages, such as material Preparation, gas sensing properties of the 3D printed sensors, and the ROV system's efficiency in navigating, detecting, and capturing CO₂. Chapter 5 provides a conclusion highlighting the key findings; it also guides future work.

Chapter 2: Literature Review

2.1. CO₂ Sensors

CO₂ sensors are divided into two main types: electrochemical, which are based on transducers, and the other is optical sensors. Optical sensors are used conventionally, but being expensive and bulky makes them unsuitable for frequent and mobile measurement. Hence, electrochemical sensors are preferred due to compactness, being inexpensive to fabricate, and versatility of the detection methods. Electrochemical sensors can be subdivided into the following categories [3]:

- Potentiometric (resistive)
- Amperometry
- Conductometric

A study focusing on Yb_{1-x}Ca_xFeO₃ nanocrystalline-based sensors prepared using the sol-gel method followed by 950 °C annealings [4] found that the best concentration was Yb_{1-x}Ca_xFeO₃ for the CO₂ sensor since it had the best response among the sensors tested. Another sensor was based on CaZnO film-coated SAW, which responded to concentration as low as 25 ppm with a response at 2.469 kHz detected at 400 was in the range of 255000 ppm [5]. Sensors made from ZnO nanowires showed good sensitivity towards CO₂ in a range of 3.8% and 3.7% for both grown and annealed, respectively. Under N₂, sensors were tested with similar results for response time and recovery time [6]. Ethylated-thiourea based sensors were tested in two variations 2a and 2b; they reached maximum signal within 30 min under the exposure. The 2b showed that it is highly selective towards CO₂ [7]. Self-standing MWCNT/Alumina composites were tested as CO₂ sensors, and they showed good sensitivity towards CO₂ with improved recovery time under ultra-violet (UV) light. The results from these studies are summarized in Table 2.1.

Mobile robots are combinations of complex mechanical and electrical systems that blend solutions from multi-disciplines, e.g., embedded control systems and mechanics [11]. The most common differential drive robots are wheel robots using the drive-

Table 2.1. Different types of CO₂ sensors and their sensitivities for specified conditions.

Sensor	Response time	Recovery time	Conditions	Sensitivity (CO ₂)	Ref.
Yb _{0.8} Ca _{0.2} FeO ₃	12 s	7 s	340 °C	Good	[4]
CaZnO, SAW	-	-	400 °C	25–5000 ppm	[8]
ZnO nanowires	≈8s	≈40s	-	3.8% CO ₂	[6]
ZnO nanowires annealed	≈8s	≈40s	-	3.7% CO ₂	[6]
2a	1 min	3 min	-	10 – 249 ppm	[7]
2b	1 min	3 min	-	10 – 249 ppm	[7]
MWCNT/alumina film	53.7 s	14.15 s	20–25 °C	-	[9]
PEI	11.7 min	20.7 min	20–25 °C	0.5% CO ₂	[10]
PEI/Starch	18.9 min	21.6 min	20–25 °C	0.5% CO ₂	[10]

steering mechanism. For autonomous driving of robotic vehicles, an open-source suite called Linorobot provides a low-cost platform for application by building on the platform. The suite supports different robots. The suite has a library that includes odometry, which is used to locate the robot's position relative to its origin. The library also calculates the linear and angular velocity from odometry data. The data collected from encoders of the motor is prone to errors due to slippage and noise. To overcome this, Linorobot used IMU with the encoder to get a more accurate reading. A robot localization package with a filter called extended Kalman filter can achieve this by using IMU readings. Full autonomy needs a high resolution with a depth parameter; a 3D depth camera or LIDAR can accomplish this. This higher resolution allows the robot to perceive the environment and avoid obstacles. Environment perception and obstacle avoidance can be done using the LINOLIDAR library [12,13]. Another project called the JPL rover project also provides an open-source library for robotic rovers. This library is a scaled-down version of the JPL rover used to explore the surface of Mars. The library has the design from off-the-shelf components and parts [14]. CO₂/CO literature review was performed in this section to pave the way for the fabrication and design of a selective and sensitive CO₂ sensor. Sensors are mostly made up of a sampling area where a chemical reaction with the material occurs. A transducer produces energy from that reaction. A signal processing unit takes the transducer signal and

produces a quantifiable electrical signal that can be displayed. The chemical reaction could produce a variety of responses such as resistance, capacitance. For CO₂ Sensing, many techniques have been established, such as potentiometric sensors, chromatography, or mass spectrometers. Relatively new methods are also being developed and used, such as infrared absorption, fiber optic sensors. The infrared absorption works by shining infrared light into the sample (air) and measuring the transmitted or reflected rays. Nevertheless, first, the rays are passed through a filter that only allows rays corresponding to the presence of CO₂ to pass, and depending on the intensity, it will quantify the CO₂ amount. The fiber optic sensor works by dipping the fiber's tip with chemicals that react with CO₂ and measuring the received signal. The intensity will indicate the CO₂ level; some material shows absorbance or reflectance changes from reaction with CO₂. Other methods have been investigated in the literature, such as sol-gel based sensors, a polymer-based array of sensors to improve the selectivity. A robotic vehicle with installed sensors to detect CO₂ molecules can be achieved by numerous sensors using thermal catalytic sensors (CAT) that react with the gas and increases the resistance in a platinum coil inside the sensor. Hence the reading of carbon emission can be obtained. Another sensing method uses acoustic wave sensors (AW) mounted on the robot; using an oscillating piezoelectric substrate can weigh the gas molecules. Acoustic sensors have a great response time over the catalytic sensor [15, 16].

2.1.1. ROV with Adsorption Technology. CO₂ gas is emitted from industrial emission streams proceeding to the atmosphere is harmful. Capturing the impurity of compounds such as physical and or chemical absorption, adsorption, membrane technology, conversion to another compound, and condensation are many capture methods. Numerous designs that have been implemented for CO₂ capturing can be broadly classified into static and movable models. The static inventions are installed on a fixed location or instruments and capture the CO₂ emission locally. Simultaneously, moving devices are free to navigate and catch the CO₂ in an entire allocated region. The moving CO₂ capturing devices are advantageous compared to static devices for their increased coverage area. However, much advancement has taken place in stationary

devices. Recently, scientists in Geneva have developed static CO₂ capturing devices installed in vehicles and cut carbon dioxide emissions by almost 90% [17]. Direct Air Capture (DAC) is a method of collecting CO₂ emission in the atmosphere [18]. Robot performing numerous activities to reduce human beings' work is highly pursued by researchers. An "air extractor" technology has been presented with offerings like no other carbon capture technology on the drawing board. Unlike conventional carbon capture and storage, the air extractors absorb carbon dioxide from any location on the planet. Hence CO₂ can be captured in nearly all significant sources from stationary factories to power plants and planes in motion. Even scientists are researching robot trees that can locally capture CO₂ and be easily installed at the desired location. At MIT, engineers have created a device to trap CO₂ that is much less energy-intensive and costly than today's technologies [19,20]. On the other hand, few reports exist on the fabrication of movable robots for capturing CO₂ emission. On a similar note, a movable air purification robot system that automatically eliminates dust and bacteria from the air while freely moving along a polluted area has been reported [21]. Compared to a blooming technology of static devices for CO₂ capture, movable robots' technology for capturing harmful gas is still in its early stage. Many opportunities are yet to be investigated.

2.2. 3D Printing

3D printing is a fabrication method based on controlled layer deposition that can print complete 3D objects using printable materials [22,23]. This fabrication method is based on the layered deposition of materials, which is also called additive manufacturing. It contrasts with the subtractive manufacturing technique where the 3D object is fabricated based on removing materials from a bulk solid. Subtractive manufacturing uses machining processes like drilling, milling, sawing, and broaching [24–26]. Sometimes 3D printing is used interchangeably with rapid prototyping. However, in rapid prototyping, fabrication can be done by either additive or subtractive manufacturing. The choice of additive or subtractive manufacturing depends on different factors like available printable material, structural complexity, cost, and the number of samples.

Usually, the complexity of the structure is the deciding factor between these two manufacturing methods. For complex geometries with solid and hollow components, the preferred fabrication method is additive manufacturing as it allows the printing of complex shapes with layer-wise deposition [27]. Alternatively, for simpler designs, the material has an important role to play. For example, for polymer-based materials, additive manufacturing is preferred, and for non-polymeric materials such as metals, woods, rocks, and so on the subtractive manufacturing is preferred [28]. Each of these fabrication methods offers its benefits and disadvantages. A summary of the technologies used in 3d printing is summarized in Figure 2.1 .In subtractive manufacturing, the samples can be fabricated in a shorter time while being cost-effective and convenient. In contrast, additive manufacturing produces less waste in terms of materials and energy and is generally more efficient [29]. Over the last few decades, 3D printing has matured as a technology. Nevertheless, it is still not being used to its full potential. It can be a cost-efficient and time-saving method for fabricating 3D objects. Recent advances in this technology allow the use of more advanced materials that can change shape once printed [30]. These new developments have opened up a new age in additive manufacturing called 4D printing. 4D printing aims to utilize the self-assembly property of 3D printed materials when exposed to specific stimuli. These stimuli can be in the form of light, pressure, temperature, moisture, and so on. In other words, 4D printing is a technology that can complement 3D printing that can allow materials to change with time while having a structure defined in terms of 3D. It is an evolving shape [31]. 3D printed objects can respond in specific ways when stimulated Using 4D printing [32, 33]. This technology is the new frontier in additive manufacturing with many potentials. It opens the path for designing shapes that can transform, adapt, and evolve in shape and properties. These printed objects will be used in different engineering and technology areas with self-assembly and transforming properties. They can be used in medical implants, electronics, robotics, energy-efficient designs, and solar technology [34–38] because of the precise and accurate geometry created with 3D and 4D printing technologies. It is possible to fabricate exact designs using 3D printing. Additive manufacturing can be used in different medical and healthcare

industries, from clinical settings to out-patient services. Using selective laser sintering (SLS), other prosthetics can be designed. They can also be used for making dental and orthopedics implants [39–41]. In these areas, the design parameters and variables can be controlled to get the desired product outcome. The mechanical and electrochemical properties can be used along with the evolving geometries to create patient-specific designs. In recent times, the trend in manufacturing is to reduce the time in designing and prototyping. This lead to advances in rapid prototyping using 3D and 4D printing. These technologies have found their automobile usage, biomedical, aeronautical, electronics, and other industries [42,43]. Furthermore, 3D and 4D printing manufacturing technologies can reduce costs by simplifying tooling and cutting material wastage. Lowering manufacturing costs is critical in highly competitive markets. With 3D and 4D printing, many industries can reduce the cost of printable objects, inventory, simplify supply chains, and increase productivity [44]. The latest developments in printing technologies include improvements in the surface condition, control, and optimization of the objects. 4D printing technology is an exciting and emerging technology for the fabrication of adaptive devices [45, 46]. Giving the designer control to combine smart Sensing and actuating materials and produce novel and versatile products. and allows researchers to make custom-designed sensors, self-assembling structures, motors, and mechanisms [47, 48]. Based on the discussion above, 3D printing is a suitable technology for designing sensors for detecting CO₂ used in this project. Figure 2.2 shows a summary of the most common used software to design parts for printing and the type of modeling system they use.

2.3. CO₂ Adsorption Materials

When carbonaceous material undergoes thermal decomposition, combustion, or partial combustion, activated carbon (AC) is produced. It is considered one of the oldest adsorbents with a large surface area [49]. The conditions of carbonization and the steps involved in this process have a considerable impact on AC's structure and geometry. The structure here means the interlayer spacing and the microcrystalline layers [50, 51]. AC is a carbonaceous material that has a surface area greater than

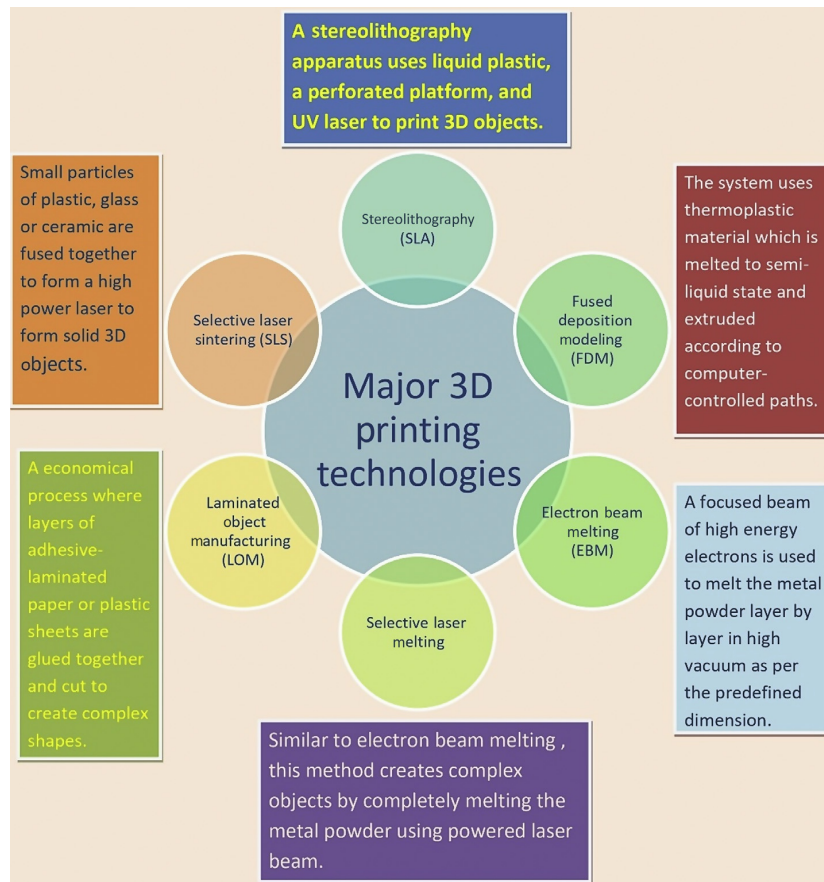


Figure 2.1. Different types of 3D printing

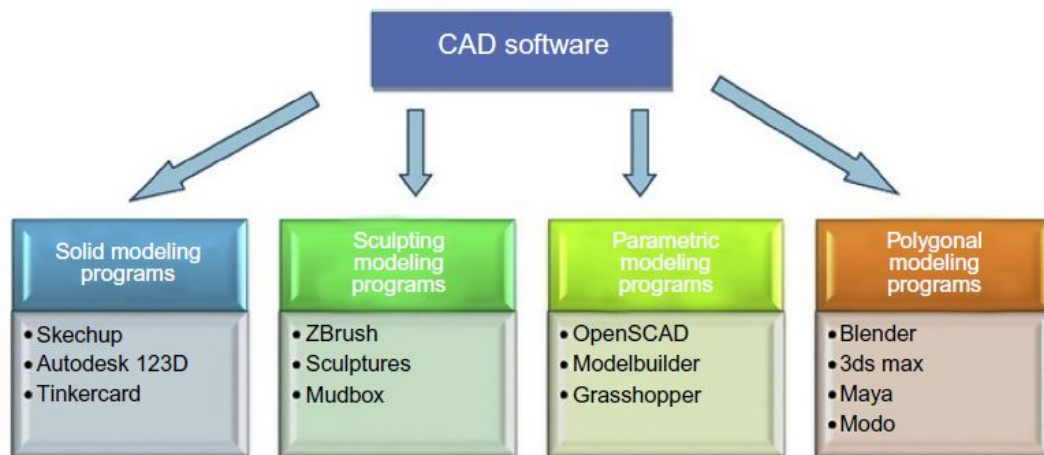


Figure 2.2. Different types of CAD software used for preparing 3D models

1000 m² g⁻¹ pores [52]]. This large surface area makes it a promising adsorbent and is used in many industries to filter out undesirable substances. The heteroatoms and defects present in the carbon structure affect the microcrystalline layers. The heteroatom attached to the carbon's edges or attached to the defect site affects the

AC's porosity. All of this is affected by the nature of the precursor [50, 53]. Another method of developing an internal surface area to get AC is introducing a stream of oxidation agents, for example, CO₂ or potassium hydroxide (KOH). It was found that the porosity is a function of the oxidation agent and temperature of the stream. The adsorption cycle's selectivity, capacity, and stability are essential in selecting the AC [54]. Adsorption characteristics and surface chemistry of AC are also affected by the metal oxide impregnation. The surface chemistry and porosity of AC affect the selectivity [55]. The carbon nanotube (CNT)-Polymer/composites are expected to blend good processability and other useful characteristics of the polymer with excellent physical and functional properties of the CNTs. According to the percolation theory using the nano dimension and high aspect ratio morphology, a low percolation threshold for the composite filler can be obtained. The CNT/polymer composites exhibit remarkable improvement of electrical conductivity by magnitudes at very low thresholds (<0.1 wt% of filler in the matrix) without sacrificing performance aspects including low weight, low melt viscosities, ease of processability. For these advantages in the present work, CNT was incorporated as nanofillers in polymer composites. However, the majority of commercial sensors use sensing materials based on WO₃, CeSnO₂ and ZnO which are n-type semiconductors for gas detection, mostly toxic gases. Although the n-type metal oxide gas sensors have some drawbacks compared to p-type metal oxide gas sensors, they also have much potential for being used in applications such as for the fabrication of CO₂ sensors. One of the differences between these two semiconductors is that the n-type metal oxide semiconductor forms an electron-depletion layer (EDL). The hole-accumulation layer (HAL) is formed with p-type semiconductor metal-oxides by adsorbing O₂ with -ve charge. Another difference is that the p-type metal-oxide-semiconductor gas sensor resistance increases when exposed to reducing target gas. The resistance of the n-type metal-oxide-semiconductor gas sensor is decreased. Moreover, most of the n-type material shows gas detection at elevated temperatures. However, there are many gaps in research for the p-type metal-oxide-semiconductor gas sensor. Hence, it is necessary to investigate the p-type metal oxide semiconductor material such as CuO for CO₂ Sensing at room temperature. Thus, to

exploit the p-type's inherent property and fabricate sensors that work at room temperature. CO_2 , CuO was incorporated as a gas sensitive material. Activation methods can be split into multiple types, for example, physical or chemical activation. For chemical activation, solid or gaseous activating agents are used [56, 57]. Streams of oxidizing agents such as CO_2 , KOH, H_3PO_4 are often used to obtain activated carbons [58]. Steam and CO_2 open pores in the internal structures by the formation of CO or H_2 [59]. The chemical activation happens by adding chemicals to open pores and achieving a higher surface area. Examples of such chemicals are KOH and NaOH, and they are then carbonized with inert gas at elevated temperatures. After the activation, the product is washed with acid and water to remove the salts, impregnated agents, and open pores [59]. Another reason behind the popularity of AC is that they have high thermal stability and are not affected by moisture in gases significantly. Stability and renewability are yet another fundamental characteristic of AC. Methods to recover the AC are temperature swing, pressure swing, and vacuum swing adsorption [60–62]. Table 2.2 shows different materials and their relative properties for adsorption of CO_2 in the literature.

AC has been made in various forms by varying its base material for formation, enhancing its adsorption capacity. Preparing AC fibers then doping them with charcoal powder (WC-ACHFs) has huge adsorption potential [63]. Improving the characteristics of mesoporous silica or any other adsorbent additives are needed. Those additives will help to tune it for specific needs. Modifying the adsorbent's surface by a functional group employing grafting or impregnation increases the adsorption efficiency and selectivity. The functional groups commonly used include Trimethoxy[3-(methylamino)propyl]silane [72], (3-Aminopropyl) Triethoxysilane [73], diethylenetriamine [73], monoethanolamine (MEA), diethanolamine (DEA) and ethylenediamine (EDA) [74]. The adsorbents could be mesoporous silica, zeolite, AC, carbon nanotubes, metal-organic framework, and silica gel, or a combination of one or the other.

Table 2.2. The following table shows the material and their relative properties for adsorption of CO₂ in the literature.

Material	CO ₂ capacity	Testing temperature	Temperature	Surface area	Adsorption re-generation	Ref.
WC-ACHF-1%	7.13 mmol g ⁻¹	273 K		1902 m ² g ⁻¹	Moderate	[63]
AC-26	4.22 mmol g ⁻¹	273 K		947 m ² g ⁻¹	Moderate	[64]
AC-28	<4.22 mmol g ⁻¹	273 K		1262 m ² g ⁻¹	Moderate	[64]
AC without K ₂ CO ₃	4.47 mmol g ⁻¹	273 K		1609 m ² g ⁻¹	Moderate	[65]
AC with 2% K ₂ CO ₃	4.36 mmol g ⁻¹	273 K		1773 m ² g ⁻¹	Significant	[65]
AC activated with NaOH	4.28 mmol g ⁻¹	273 K		1149 m ² g ⁻¹	Moderate	[66]
AC-540	5.25 mmol g ⁻¹	273 K@100 kPa		892 m ² g ⁻¹	Moderate	[67]
AC-680	6.47 mmol g ⁻¹	273 K@100 kPa		1350 m ² g ⁻¹	Moderate	[67]
AC-820	5.41 mmol g ⁻¹	273 K@100 kPa		1763 m ² g ⁻¹	Moderate	[67]
MWTAC	108.97 mg g ⁻¹	-		11.80 m ² g ⁻¹	Moderate	[68]
WTAC	87.42 mg g ⁻¹	-		256.45 m ² g ⁻¹	Moderate	[68]
MSN 65% PEI	160 mg g ⁻¹	353.15 K		13.6 m ² g ⁻¹	Poor	[69]
SBA-15 65% PEI	105 mg g ⁻¹	353.15 K		-	Poor	[69]
HMS 70% TEPA	5.82 mmol g ⁻¹	348.15 K	15%	4.24 m ² g ⁻¹	Poor	[70]
SBA-15 4.7% G-Si silica with TEPA	6.02 mmol g ⁻¹	423.15 K		-	Poor	[71]

2.4. ROV Navigation

In this era of automation, robots have taken over much of the laborious tasks in industrial processes. Traditionally, people used to work in assembly lines doing monotonous tasks. Robots have replaced people for these jobs as they work faster and more efficiently and with higher safety. The new era of robotics is geared towards making them intelligent and make decisions like humans. Much development has gone into artificial intelligence with the availability of big data and significant leaps in computational processing power. One of the challenges in mobile robots is path planning. This problem is deeply ingrained with robot navigation. The robot has to move from an initial position to a destination and accomplish tasks such as avoiding obstacles or carrying tools. Robots such as drones, autonomous vehicles, wall-climbing robotics, and underwater vehicles are designed with different algorithms to accomplish various

tasks in these environments [75–78]. During the early stage of development, roboticists focused on 2-dimensional path planning. They utilized nature-inspired algorithms [79]. In the current stage, more sophisticated algorithms have been developed for robot motion. Navigation is vital in the field of mobile and autonomous robotics. Currently, many robots are designed that have intelligent algorithms. They are intended to be used in various areas, such as industry, transportation, rescue, and surveillance. One of the challenges in navigation is path planning. Path planning requires the calculation of a collision-free path from source to destination subject to a constraint. This constraint can be minimizing the cost related to that path, such as distance traveled or energy used. Based on the environment, the path planning problem can be categorized as either static or dynamic. When obstacles do not alter their locations over time, it is called static path planning. Whereas, if obstacles alter their orientations and locations over time, it is considered dynamic path planning. Robots can know the information about their paths through two main ways: online and offline methods. In online path planning algorithms, the data about the surroundings is obtained by a sensor installed in the robot. The robot uses the data to construct a map of the environment and do the necessary computation to find the optimal path. In offline path planning, a pre-captured map of the area is installed to the robot memory, and usually, the path can also be programmed if the obstacles are static. Researchers used a combination of Particle Swarm and Modified Bat algorithms to map the robot's paths in static and dynamic environments [80]. They applied a multi-objective function that the robot used to accomplish its goals, such as using the shortest distance and path smoothness. For avoiding obstacles, they used the gap vector method. [81] planned the path in a disorganized environment by using the free segment and turning point algorithm. The turning point method looks for a safe path without obstacles for the robot from the initial point to endpoint without having collisions. Furthermore, the sliding mode controller was used for stabilizing the robot that aided in tracking the optimal trajectory. Their method tackles two goals for the robot, including path safety and path distance. To solve a multi-objective path planning problem for mobile robots, [82] used the firefly and the chaotic particle swarm optimization (PSO) algorithms. Researchers

in artificial intelligence (AI) are interested in understanding and making robots intelligent. Part of this includes helping robots improve performance by making the right decisions. An intelligent system requires algorithms to solve problems. Some commonly used algorithms in artificial intelligence include Neural Network (NN), Fuzzy logic system, Genetic Algorithm (GA), Ant Colony Optimization (ACO), and Particle Swarm Optimization. Researchers use a combination of these different algorithms and real-time data from sensors to aid the robots in making optimal decisions in solving the path planning problem. These sensors can include light detection and ranging (LiDAR), depth camera, infrared camera, and ultrasonic sensors. The following section discusses some of these sensor technologies that will be used in our robot vehicle.

2.4.1. LIDAR. LiDAR is a technology for measuring distances by hitting the target with a laser beam and measuring the reflection time with a sensor. Differences in laser return times and wavelengths can make a digital 3D representation of the target and the surrounding environment or obstacles. It has applications in all mobile robots, including autonomous vehicles. LiDAR sensors are used for making high-resolution maps. In path planning and navigation problems, LiDARs are usually used to control the robot's orientation and position. They can be used alone or combined with other sensors such as GPS and camera. Multiple sensors working together with good algorithms can give better results. Combined with a camera and LiDAR, a mobile robot system can be deployed to map the local environment, ensuring that the mobile robot can automatically locate and identify landmarks and correct their position and orientation. This technique is called SLAM which is short for simultaneous localization and mapping.

2.4.2. Kinect 360 Depth Camera. The Kinect 360 is a Microsoft product initially made for the Xbox 360 to enable users to play games by moving the body, and the sensor would detect their movement. However, due to the sensor's price and ease of development, many in the robotics community developed libraries to use the sensor in various applications. As shown in Figure 2.3, the sensor features an IR camera and projector to get the depth data and a standard RGB camera with a motorized

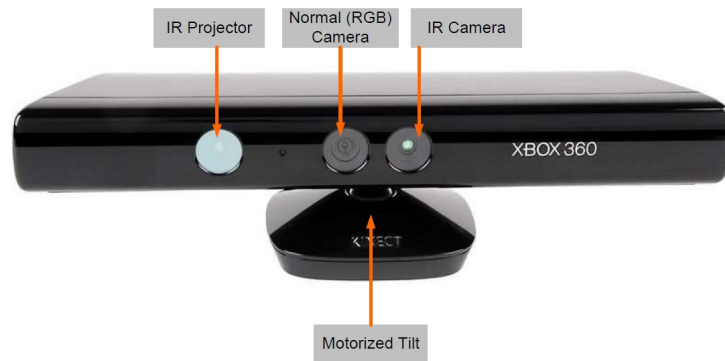


Figure 2.3. Showing the core parts of Kinect [83]

tilt to change the sensor's orientation. One of the sensor's many applications is 3D scanner, which depends on the IR camera's depth data. Another use in the Robot Operating System (ROS) is that robots use Kinect as a mapping sensor to avoid obstacles and plan paths. The downside to the Kinect sensor other than the relatively low resolution is that the IR sensor does not work in the outdoor environment due to external interference (The Sun). Whence, the combination of a LiDAR would create a versatile sensing setup.

2.4.3. Robot Operating System. There are many different types of sensors, controllers, and actuators available in the market. In developing a robot that enables quick communication between these different sensors from different manufacturers, a dedicated system was designed to be known as the Robot Operating System (ROS). Unlike a full operating system such as Windows, Mac, or Linux, it is a robotics framework. It allows abstraction of the hardware and permits low-level device control, message-passing between processes, implementation of commonly-used functionality, and package management. ROS-based processes take place in nodes that are represented in a graph architecture. These nodes perform computations and post and receive messages, control, state, plan, actuate the sensors. ROS allows different sensors to be easily added to the robot and allow additional features to be added due to its modular nature. It is a global collaborative effort that is improving the development

of robotics research. Our robot will run on an open-source Unix-like operating system. ROS will run on top of that and allow complete control and integration of the robot and its sub-components.

2.5. Characterization Techniques

The surface morphology, structural information, and optical properties of synthesized materials are significant before using them for any application. This section briefly introduces various characterization techniques like; XRD, SEM, TEM, EDS, PL, stylus profiling, and UV-Vis-NIR spectroscopy, I-V studies available to identify the material properties. It also covers a brief description of the photoconductivity measurement setup adopted in the present work to analyze fabricated PDs.

2.5.1. X-Ray Diffraction. The X-ray diffraction is a non-destructive and standard tool that provides information about the crystal structure, size of crystallites, crystallographic phase, unit cell dimensions, and materials composition. Each material has its unique XRD pattern, which acts like a fingerprint to recognize the material. As a result, the XRD technique is used to identify materials by comparing the obtained XRD pattern with the reference pattern. X-rays are electromagnetic (EM) radiation in the wavelength range 0.02 Å to 100 Å. However, the X-ray having a wavelength in the region of a Å to 0.1 Å are used for X-ray diffraction. As X-ray wavelength is analogous with an atom's size, they are suitable for exploring the material's structural arrangement.³ X-rays are generated when high-speed electrons fall on the heavy metal crystal such as Cu, Al, Mo, and Mg. When a high-speed electron collides with a metal crystal at a high positive potential, it gets deflected from its path due to the Coulomb force between the moving electron and the target atom's nucleus. The scattered electron loses its energy, and this decrease in energy results in X-ray emission, as shown in Figure 2.4(a). The scattered electron may further have the second collision with another target atom, causing the second X-ray emission. This process of electron scattering continues until the electron becomes approximately stationary. The photons generated in this process form a continuous X-ray spectrum, as shown in Figure 2.4

(b). The continuous X-ray spectrum has a cut-off wavelength (λ_{min}) below which X-ray spectrum does not exist, and it is independent of the target material. If the initial energy of the electron is K_0 (eV) Furthermore, during the nuclear interaction, it reduces to ΔK , producing an X-ray of energy $h\nu$ then the minimum possible wavelength is defined as:

$$\lambda_{min} = \frac{hc}{eV} \quad (2.1)$$

Where e is the elementary charge, c is the speed of light, h is the Planck's constant, and V is the voltage by which electrons are accelerated.

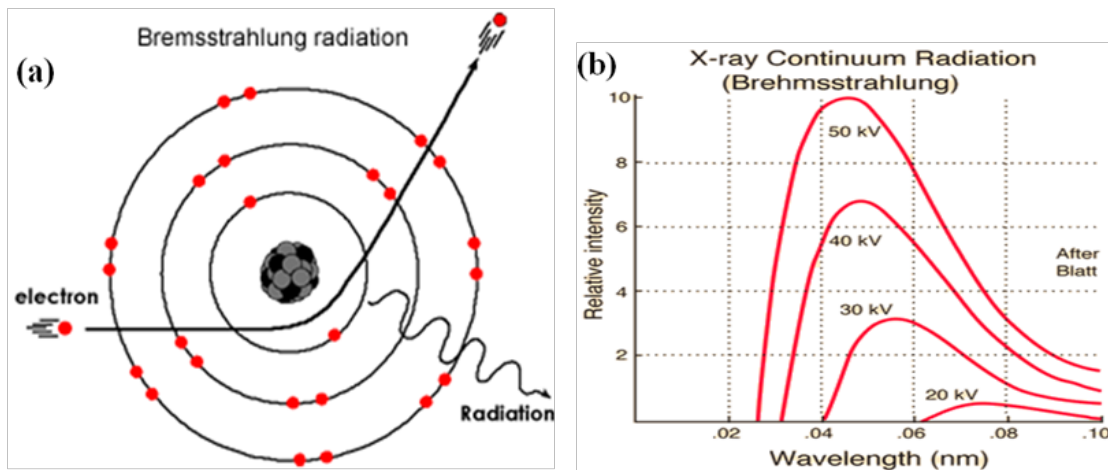


Figure 2.4. (a) Electron scattering process. (b) Continuous X-ray spectrum at different target potential.

From Equation 2.1, the wavelength of the produced X-ray is inversely proportional to the applied potential. Thus with an increase in applied voltage, the continuous X-ray spectrum shifts towards the lower wavelength, as shown in Figure 2.4(b). Further, the bombarding electron can also eject the inner shell electron of the target metal atom. An upper energy level's electron fills the unfilled vacancy. This process results in an X-ray of finite energy, equivalent to the energy change between the target atoms' energy levels. The Characterization process of X-ray diffraction is as follows; the sample is placed in the sample holder, and the sample is subjected to the monochromatic X-ray (i.e., λ is fixed; generally $\lambda = 1.541 \text{ \AA}$), which is generated within the X-ray tube. The incident radiation interacts with atoms' electrons in a crystal and creates

an oscillating electric field of frequency equivalent to the incident beam. Hence, the electrons coherently scatter the incoming electromagnetic radiation (X-ray). The constructive interference is formed if the scattered beams are in phase, and maximum intensity is achieved at a particular angle. Process for characteristics X-ray and the characteristics of X-ray lines along a continuous spectrum are illustrated in Figure 2.5 (a) & (b).

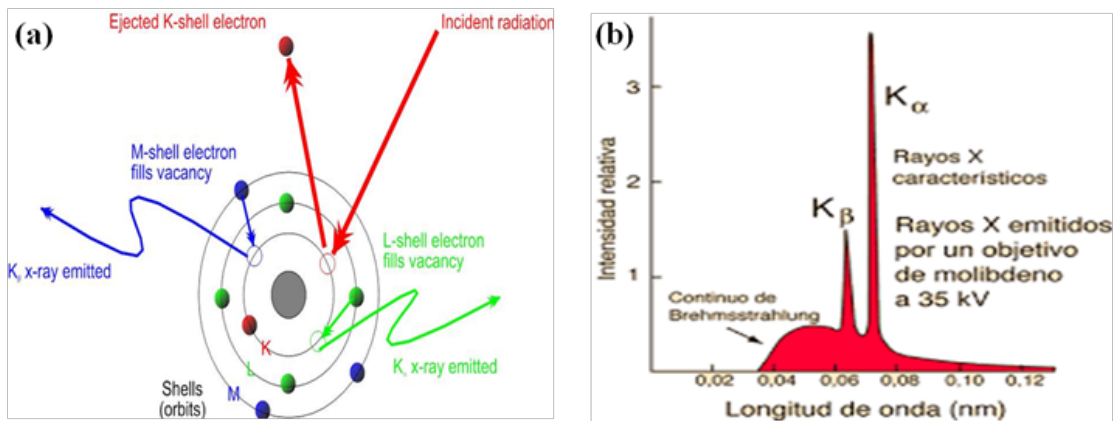


Figure 2.5. (a) Process of characteristics X-ray. (b) Characteristics X-ray lines along a continuous spectrum.

Bragg's law defines the constructive interference of X-ray scattered by the crystal:

$$n\lambda = 2d_{hkl} \sin(\theta_{hkl}) \quad (2.2)$$

Where n represents the order of the reflection, λ corresponds to the wavelength of the incident X-ray beam, $[hkl]$ is lattice plane in a solid crystalline material, d_{hkl} relates to the inter-planer spacing in a crystal and θ_{hkl} relates to the angle of incidence (Bragg's angle). A schematic representation of Bragg's law of diffraction is shown in Figure 2.6.

Further, the XRD pattern is plotted between intensity and Bragg's angle. The XRD peaks can be characterized by their intensity, profile, and position. The peak position depends upon the periodic arrangement of atom/molecules in the crystal. The intensity of the peak gives information about the crystalline structure and preferred

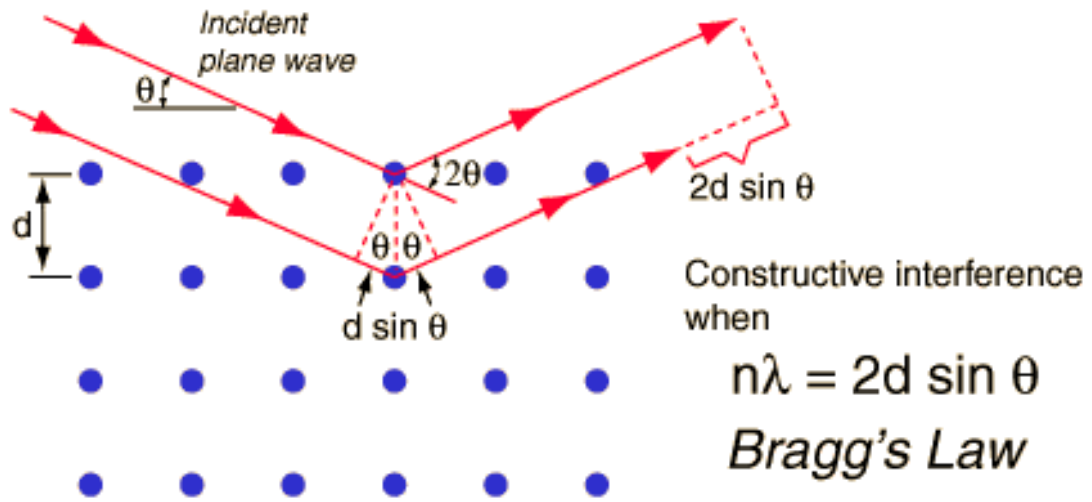


Figure 2.6. Schematic for Bragg's law of diffraction.

orientation of the sample. The profile of the XRD peaks describes the strain in the material. Moreover, the crystallite size is estimated by the Debye-Scherrer equation given below:

$$D = K\lambda\beta \cos(\theta) \quad (2.3)$$

Where K represents Scherrer constant with a value of about 0.89, θ represents corresponding Bragg's position, and β represents full width at half maxima (FWHM) of the diffraction peak in XRD pattern.

2.5.2. Scanning Electron Microscopy. SEM is a surface technique that captures a three-dimensional high-resolution image of the sample and gives information about the material morphology. The SEM has high resolution than optical microscopy and permits morphological observation in the nanometre regime. The resolution (R) of the microscope is given by Equation 2.4.

$$D = \frac{\lambda}{2n_r \sin(\alpha)} \quad (2.4)$$

Where λ represents the wavelength used in the microscope, n_r represents the refractive index of the medium between lens and object, and α represents semi-angle subtended

by the aperture. In an optical microscope, visible light is used as a source, which is not sufficient to characterize a material having nanostructure morphology. On the other hand, in SEM accelerated electron beam having wavelength 10⁵ times smaller than the light is used, which intern causes an increment in the resolution. Figure 2.7 shows the schematic illustration of SEM analysis. In SEM, the electron beam is produced from the filament called an electron gun. Materials like tungsten or lanthanum hexaboride (LaB₆) are used for electron gun but frequently used is tungsten hairpin gun. The electron beam generally has an energy between a few keV to 15 keV; the electron beam remains attached to the anode. The electron beam passes through a condenser lens and gets condensed, which is now focused on the sample with an objective lens's help. A pair of scanning coil deflects the beam either linearly or in raster order over a circular region of the sample surface, placed above the objective. The deflection of the electron beam is controlled by varying applied voltage of the scanning coil. For SEM analysis, the sample must be in a vacuum and electrically conducting. If the sample is non-conducting, it should be conducted by coating a thin film of conducting materials like gold or carbon.

When the electron beam strikes the sample surface, it causes the emission of secondary and backscattered electrons along with characteristic X-rays emissions from the surface of the sample. The secondary electrons emitted from the sample are collected by a secondary detector or backscattered detector and translated to a signal. The signal is amplified, analyzed, and translated into an image. The image comprises thousands of different intensity spots on the monitor screen related to the sample's morphology.

SEM is used to examine both morphologies ("size and shape") and topography ("how it looks") of the sample. Moreover, the orientation of grains in the sample can also be examined using high-resolution SEM. The backscattered electron has nuclear interaction and high energy secondary electrons; the resolution in backscattered electron images lies typically within the range of 25-100 nm. The resolution of the secondary electron image is typically in the range of 1-5 nm. Moreover, the secondary electron image resolution is considerably better than the backscattered electron im-

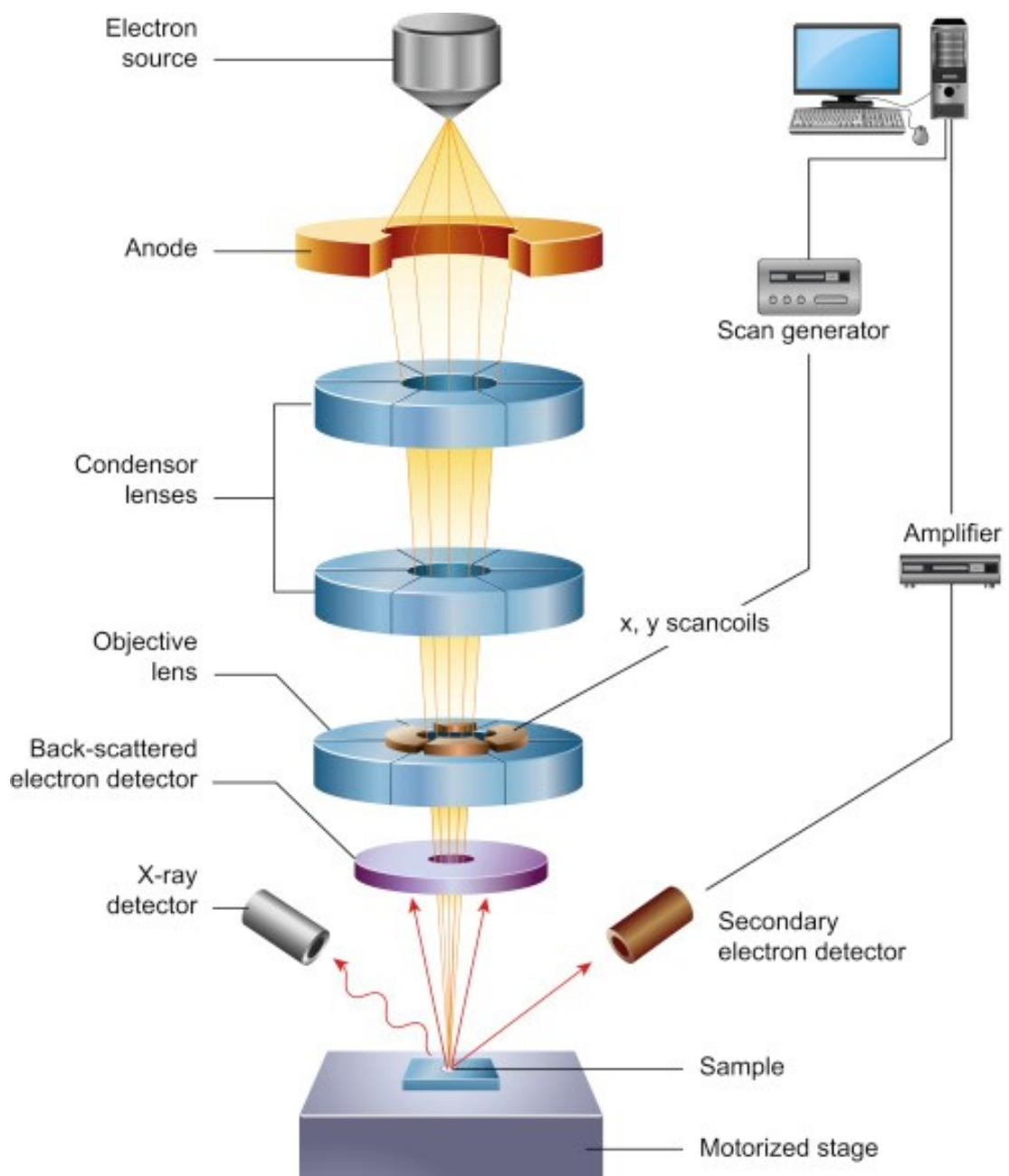


Figure 2.7. Schematic for SEM analysis. [84]

ages because of the shorter penetration depth. Nowadays, a field-emission cathode is utilized as an electron gun in a scanning electron microscope. The field emission gun equipped SEM is called Field Emission Scanning Electron microscope (FESEM). The FESEM possesses a high resolution concerning the conventional SEM. Furthermore, FESEM provides clear, lesser electrostatically distorted images with a spatial resolution

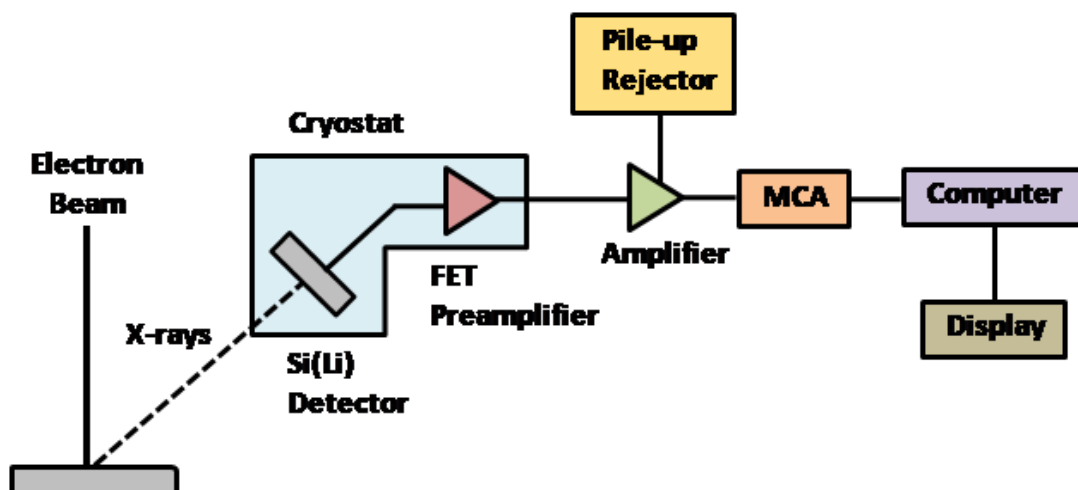


Figure 2.8. Schematic of energy dispersive X-ray setup.

(three to six-time better) than convention SEM. The basic principle of x-ray setup is shown in Figure 2.9.

2.5.3. Fourier-transform Infrared Spectroscopy. FTIR works on the principle that the bonds and group of bonds vibrate at different characteristic absorption frequencies. Each molecule absorbs infrared energy at different frequencies when introduced to infrared rays. The electric charge of its atom generates the electric dipole moment of a molecule. An excitation to higher vibration states occurs when molecules with an electric dipole moment permit infrared photons interaction. The infrared spectrum of absorption for solid, liquid, or gas can be acquired using the FTIR approach. FTIR spectrum is used to record high spectral resolution data for a broad spectral range simultaneously. In reality, the word Fourier transform infrared spectroscopy depicts that the raw data is transformed into an actual spectrum by applying a mathematical process called Fourier transform. The basic principle is shown in Figure 2.9.

The infrared radiation, which is a part of the electromagnetic spectrum, comprises three distinct regions: near, mid, and far IR. The near-infrared radiation is in the wavenumber range of $14000\text{--}4000\text{ cm}^{-1}$ ($0.8\text{--}2.5\ \mu\text{m}$), and it helps in the excitation of harmonic vibrations. The mid-infrared radiation is in the wavenumber range of

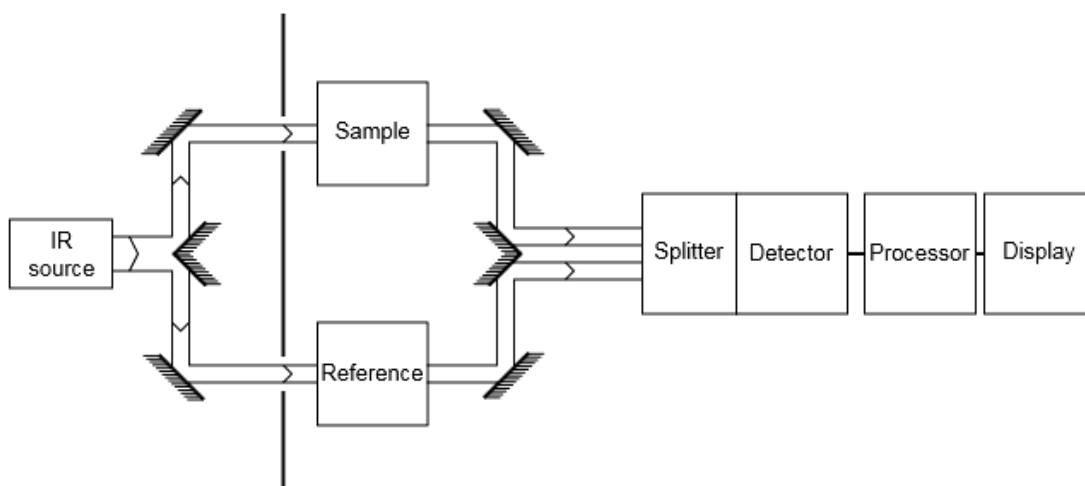


Figure 2.9. Block diagram of a FTIR spectrometer [85]

$4000\text{--}400\text{ cm}^{-1}$ ($2.5\text{--}25\text{ }\mu\text{m}$), and it is used to determine the fundamentals vibrations and rotational-vibration modes related to it. Lastly, the far-infrared radiation region has low energy, situated beside the microwave region in the wavenumber range of $400\text{--}10\text{ cm}^{-1}$ ($25\text{--}1000\text{ }\mu\text{m}$), and is used for rotational modes.

2.5.4. Current-Voltage (I-V) characteristics. It is imperative to precisely measure the material's conductivity, as this parameter helps to study the device's performance or the composition of a material. Different methods are implied to measure the material's conductivity depending on the material type (bulk sample or a thin film). For bulk samples, a two-point measurement using a low-cost ohmmeter is the easiest method to determine the material conductivity. However, it can only be used for large samples, and its precision is limited. The correlation of electric current and voltage (potential difference) is usually plotted in a graph, and this correlation is referred to as current-voltage (I-V) characteristic. The resistance and the sample size should be precisely measured, as this will affect the bulk sample's conductivity. The material's resistance is defined as the ratio of applied voltage through the material to measured current or measured voltage through the material to current-driven across the material.

Resistance (R) is directly proportional to resistivity (ρ) and is represented as follows:

$$R = \rho L/A \quad (2.5)$$

Where L is the length of the homogeneous bar, and A is the uniform cross-sectional area. I-V characteristic curve provides an insight into the behavior of electronic devices. These devices include junction field-effect transistors (JFETs), heterojunction bipolar transistors (HBTs), bipolar junction transistors (BJTs), and several types of diodes such as rectifying, laser, Schottky, Zener, light-emitting diodes, and many more. I-V characteristics of the samples investigated in the present thesis have been studied using a Keithley 65487 source meter interfaced with a PC using a GPIB port shown in equation 2.5 [86,87].

2.5.5. Thermogravimetric Analysis. Thermal stability of a material and the percent of volatile components in the material are measured with thermogravimetric analysis (TGA) by measuring the difference in the sample's weight, which arises when the sample is heated at a uniform rate. The thermogravimetric analyzer is equipment that is used for thermogravimetric analysis (TGA). As the sample temperature is altered over time, a thermogravimetric analyzer's mass change is measured. The base measurements in the thermogravimetric analyzer are temperature, time, and mass. Furthermore, numerous measurements can be obtained from these three base measurements. In general, a thermogravimetric analyzer consists of a sample pan situated within the furnace and an accuracy balance attached to a program that controls the temperature. A thermal reaction occurs when the temperature is increased at a uniform rate or kept stable for a constant mass decrease. A thermal reaction occurs at high, constant, or controlled pressures and even at high vacuum pressures. The thermal reaction also occurs at different atmospheres such as inert gas, ambient air, vacuum, corrosive gases, carburizing gases, oxidizing and reducing gases and vapors of liquids. Mass or percentage of the initial mass (Y-axis) vs. temperature or time (X-axis) is plotted using the thermogravimetric results obtained from the thermal reaction. This graph is usually leveled and is called a curve. Inflection points can be obtained

by plotting the first derivative curve of the TGA curve. The DTG curve is helpful for in-depth interpretations and differential thermal analysis.

Chapter 3: Materials and Methods

3.1. Materials

The primary materials used for fabricating the CuO/SWCNT nanocomposite are as follows:

- 99.99% pure CuO powder (molecular weight 79.55) from Sigma Aldrich, Germany for € 204 per pack of 25 g.
- $\geq 95\%$ CNT (Single-walled (6,5) chirality, 0.78 nm average diameter) from Sigma Aldrich, Germany for € 1080 per pack of 1 g.
- $\geq 99.99\%$ pure Ethanol (puriss. p.a., absolute, GC, molecular weight 46.07) from Sigma Aldrich, Germany for € 330 per pack of 2.5 L.

The 3D printed sensors are fabricated from LCD-C resin that is obtained from Sparkmaker.

3.2. Preparation of Nanomaterial (CNT/CuO) and Resin Nanocomposite (Resin/CNT/CuO)

The nanocomposite of CuO with single-wall carbon nanotube (SWCNT) was synthesized by the hydrothermal method, as shown in Figure 3.1. 0.1 g of CuO (T0) and 0.01 g SWCNT (purity $>95\%$) were added to the mixture of water (60 mL) and ethanol (30 mL). The solution was sonicated for 4 h. Then it was autoclaved at 120 °C for 12 h in a 100 mL autoclave bottle. Then, it was centrifuged at 4000 rpm for two hours. The product was dried at 60 °C for 12 h. The obtained solid was labeled as CuO/SWCNT.

The unique properties of CNT combined with their high dimensional ratio (micrometer scale length /nanometer diameter) and low density (theoretical $\approx 1.3 \text{ g cm}^{-3}$) have brought about extensive research in creating CNT-polymer composite material to take advantage these properties. The carbon nanotube (CNT)-Polymer/composites are expected to blend good processability and other useful characteristics of the polymer with

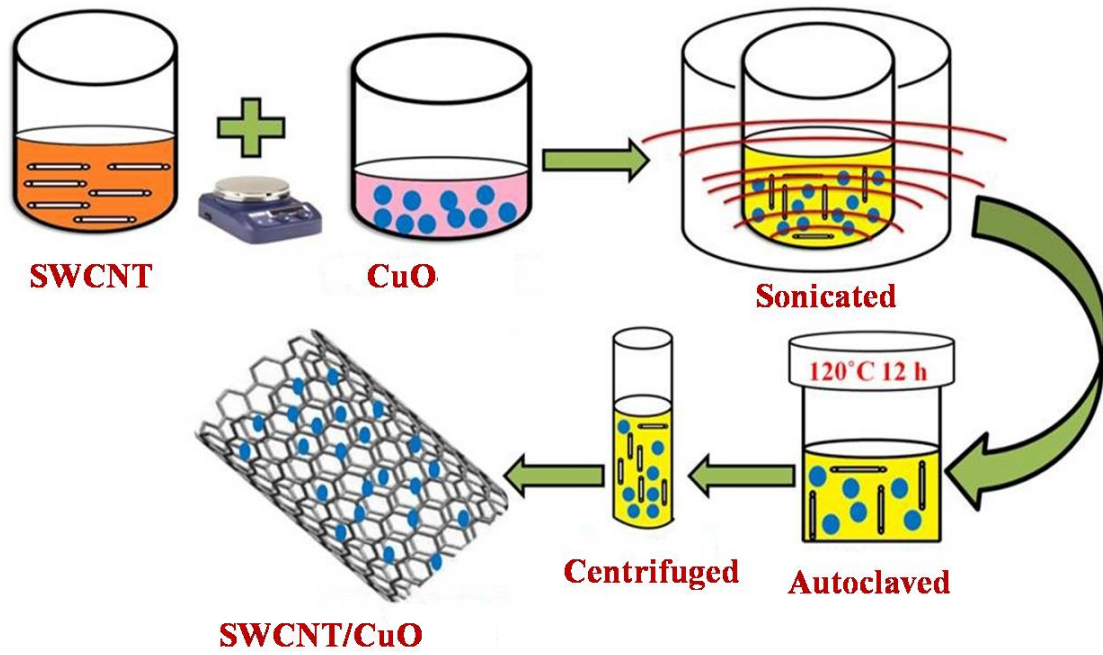


Figure 3.1. Schematic representation of SWCNT/CuO nanocomposite preparation via hydrothermal method.

excellent physical and functional properties of the CNTs. According to the percolation theory using nano-dimension and high aspect ratio morphology, a low percolation threshold for the filler in the composite can be obtained. For these advantages in the present work, CNT was incorporated as nanofillers in polymer composites. In the present work, CNT/CuO is used as a gas sensitive material. Researchers are paying attention to the metal oxide semiconductor-based gas sensors due to their high sensitivity, more straightforward measurement methods, low fabrication cost, and signal characteristics. CNT's mechanical and physical properties, combined with their high aspect ratio and low density, have brought widespread research fabricating CNT-polymer composite material to take advantage of those properties.

3.3. 3D Printing

3.3.1. Material Preparation for 3D Printing. The sensing material prepared by mixing CNT 2 wt% with PU UV cured. Any higher concentration will result in unprintable material due to high opacity, where the UV light could not penetrate to cure the layer. The mixture stirred mechanically for 5 hours in an ice bath. While stirring, the mixture was kept in a dark environment to prevent curing. The mixture

was then kept under vacuum to remove air bubbles introduced during mixing. The material is then put in a small tank (7E4 cm). The smaller tank is used to reduce waste resin and filler material (graphene). The tank is put in the DLP printer to start the printing process. Autodesk Fusion 360 was used to prepare a model of porous material with channels of 0.13 mm with a distance of 0.13mm in between and a material inspired by metal foams. The material's size was a cube with $1 \times 1 \times 1 \text{ cm}^3$, a printer with the DLP printer, then the electrodes were added to it.

3.3.2. 3D Printing Process of CNT/CuO Nanocomposites. In the present work, the digital light processing (DLP) based 3D printing technique is adopted for fabricating gas sensors. The DLP-based 3D printing enables the creation of 3D parts via photopolymerization of UV curing resins. UV light is focused on a liquid polymer through a projector window that controls the 3D objects layer printing structure. The polymeric resin consists of monomers and or oligomers and photoinitiators, triggering the polymerization reaction. Curing can occur in many ways, like the production of free radicals, the generation of cationic species, and other pathways. For 3D printing of the R&D-oriented objects, specific parameters like printer design, print settings, and photopolymer composite properties have to be investigated optimized. Figure 3.2 shows the various challenges that need to be overcome before initiating the printing.

The CuO wt% was taken as fixed for all the composite formation, i.e., and CNT wt% in resin is varied from 0.52.5 wt%. The CNT wt % variation, is done to achieve a partially conducting network within the 3D printed design. Initially, 10 of resin is taken, and 0.1 wt% CuO is added along with CNT by varying the CNT concentration from 0.05-0.25 wt%. The schematic representation of the CNT/CuO/Resin composite synthesis is shown in Figure 3.3. Initially, the composite mixture is subjected to ultrasonication in an ice-cold bath for 1hours After that; the composite is stirred using a magnetic stirrer at 600 RPM in an ice-cold bath for 12 hours. The hour of stirring ensures the homogenous dispersion of CNT/CuO nanostructure in the matrix of resin. The as-synthesized solution was further taken for DLP based 3D printing. Figure 3.3 shows a representative workflow for the synthesis of CNT/CuO/resin composite for DLP based 3D printing.

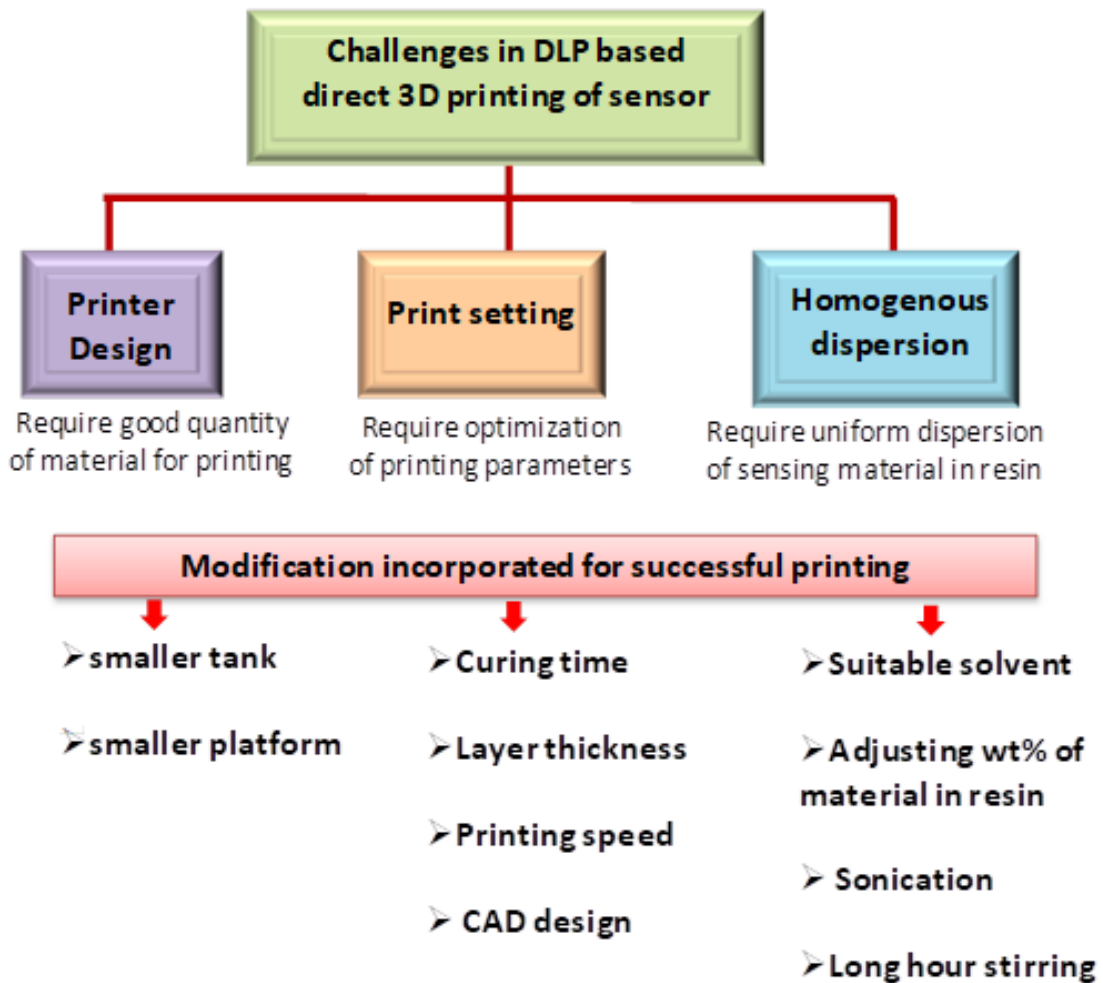


Figure 3.2. : Schematic showing the various challenges DLP based 3D printing of the sensors and modifications incorporated to overcome these limitations.

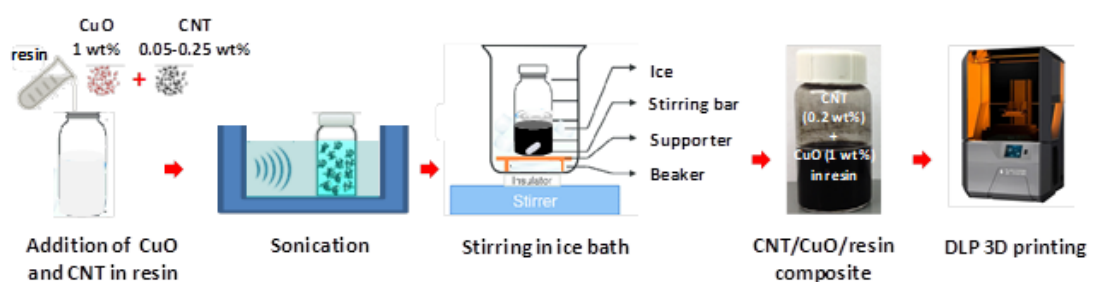


Figure 3.3. Schematic representation of the synthesis of CNT/CuO/resin composite for DLP based 3D printing

New Printer Tank Design Challenges. The commercially available DLP printer comes with a larger tank and larger printing platform. The inbuilt tank requires a minimum quantity of the resin (100 ml) to initiate the printing. While using the

inbuilt tank during parameter optimization of 3D printed sensors, a large amount of nanostructured material has to be added, which results in the waste of the material and is economically not feasible. To overcome this, we have incorporated certain modifications in the DPL 3D printer, as shown in Figure 3.4. A smaller tank was fabricated by sticking the small plastic box on the tank's plastic film, as shown in figure 3.3a. The edges of the smaller tank stuck to plastic by using a sticky silicone gel. The smaller tank's incorporation to initiate the 3D printing of the objects with a minimum volume of 10 ml. the small tank drastically reduces the composite material's consumption by ten folds. For printing with the smaller tank, the printing platform also needs to be modified accordingly. A smaller printing platform was made with the hollow steel block fixed to the original platform with the screw, as shown in Figure 3.4b. An array of holes was made in the printing platform to offer the resin's smooth flow during the platform's downward printing movement and lift-off.

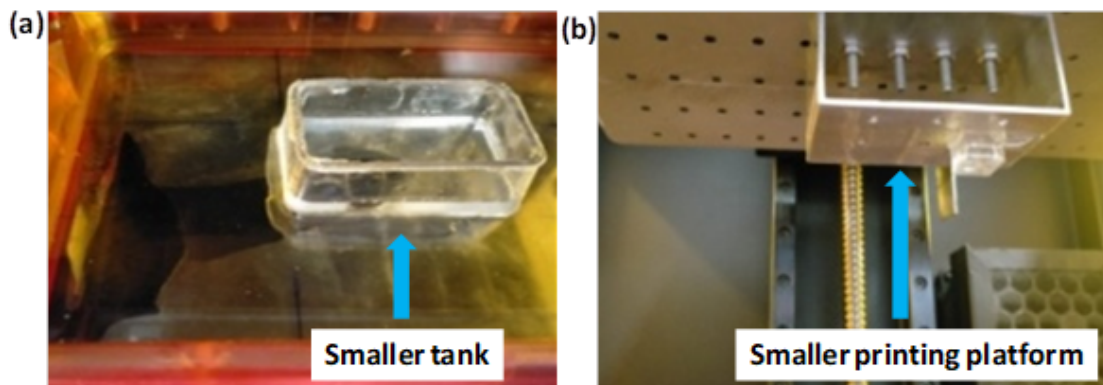


Figure 3.4. Modifications in DLP 3D printer. (a) Designing a smaller printing tank. (b) Designing a smaller printing platform.

Optimizing Paramters for 3D Printing. Critical printing parameters need to be adjusted appropriately to initiate the 3D printing of the nanocomposite materials. The various essential printing parameters include:

- Layer height
- UV Light intensity
- UV Light exposure time

- Print speed

For instance, photoinitiators' absorption coefficient and mixed CNT (which generally inhibits the polymerization process) are factors to initiate polymer network formation. Geometrical limitations, restricting the volume of the photocurable polymer, also alter the curing kinetics. The nanostructures in the prepolymer resin can introduce geometrical in addition to heterogeneous constraints and interfaces, influencing polymer networks' development throughout photopolymerization. Initially, 3D printing was initiated with composite having the highest CNT concentration, i.e., 0.25 wt%. Upon printing the CNT (0.25 wt %)/CuO (1 wt %)/resin composite with the default print settings, only the first four layers were printed on the platform during the complete print, as shown in Figure 3.4. This could be due to variation in the first four layers' exposure time and the rest of the default print settings layers. The first four layers have an exposure time of 80 seconds compared to the exposure time of 20 seconds for the rest of the layers, as shown in Figure 3.5. The addition of the CNT in the resin acts as a light scattering center; thus, the resin does not cure entirely and needs more curing time for a shorter duration of light exposure.

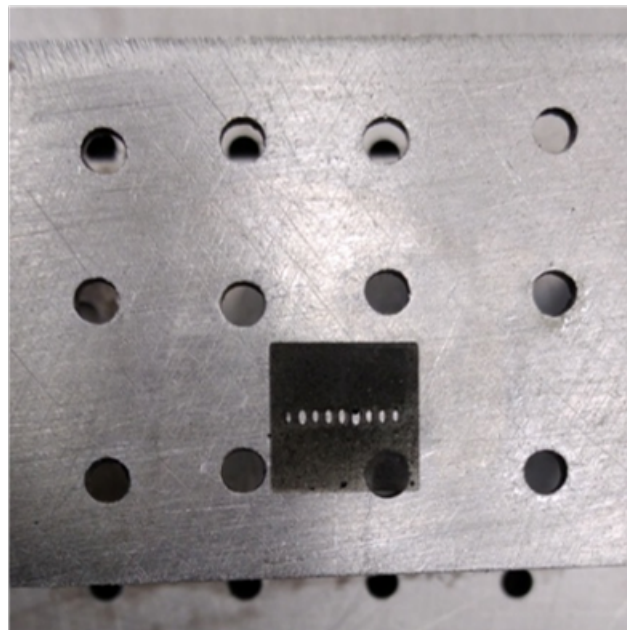


Figure 3.5. The first four printed layers with light at exposure time of 80 sec

The exposure time was increased to 150 seconds to ensure the composite polymer's curing. While printing with an exposure time of 150 seconds, the structure printing, the issue of delaminating the object from the tank was noticed, as shown in Figure 3.6. Even the 3D printed object layers were observed to be delaminating easily with mild sonication. This could be due to some uncured polymer within the thickness of each layer. The CNT present in the composite may not allow light to pass through the entire thickness of the layer and some of the polymers remains uncured, which results in the easy breaking of the object.; the layer thickness of the object was reduced to 0.035 mm from the initial layer thickness of 0.05 mm to overcome the breaking of the print.

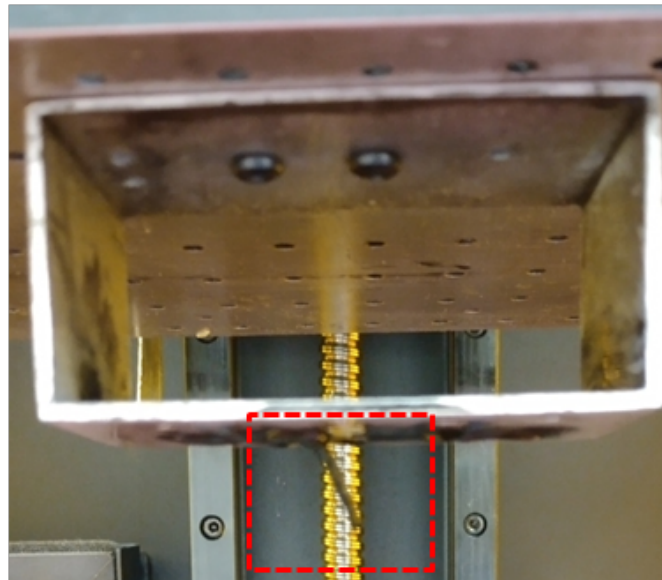


Figure 3.6. Delamination of the 3D printing object.

After adjusting the layer thickness to 35 and exposure time to 150 seconds, the CNT(0.25 wt %)/CuO (1 wt%)/resin composite object was successfully printed, as shown in Figure 3.8. The few broken lines observed in the Figure are created during the time of breaking.

After optimizing the sensor composite's 3D printing parameters, an array of the sensing pad was printed with an established print setting. During the array's printing, as the 3D printing object's size increases, a nonuniformity in the print structure was

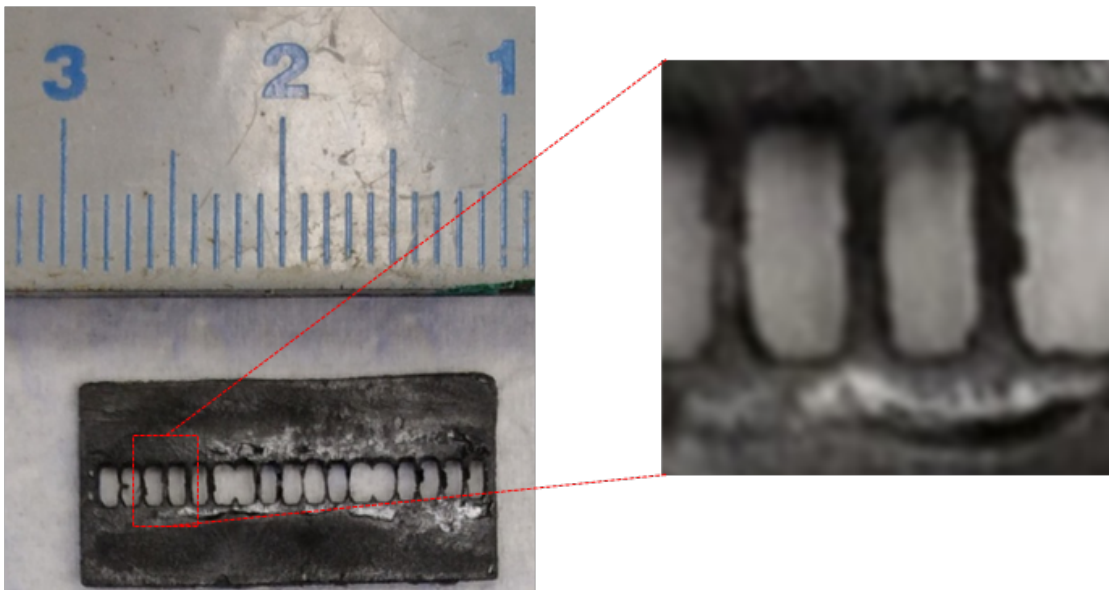


Figure 3.7. 3D printed CNT(0.25 wt%)/CuO (1 wt%)/resin composite

observed. The object was not printed uniformly on the platform, as shown in Figure 3.7. the nonuniform print could be due to the excess scattering of the light off CNT that hinders the resin's cure during printing.

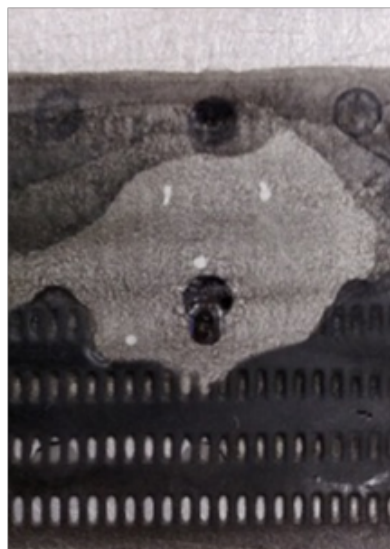


Figure 3.8. Non-uniform printing of composite material.

On the other hand, a decrease in the CNT concentration from 0.25 to 0.2 wt%

resulted in less scattering if the light and the sensor array were successfully printed. Figure 3.9 shows the 3D printed array of sensor pad after uniform dispersion of the CNT (0.2 wt%)/CuO(1 wt %) in the resin matrix with an exposure time of 150 seconds and a layer height of 0.035mm.

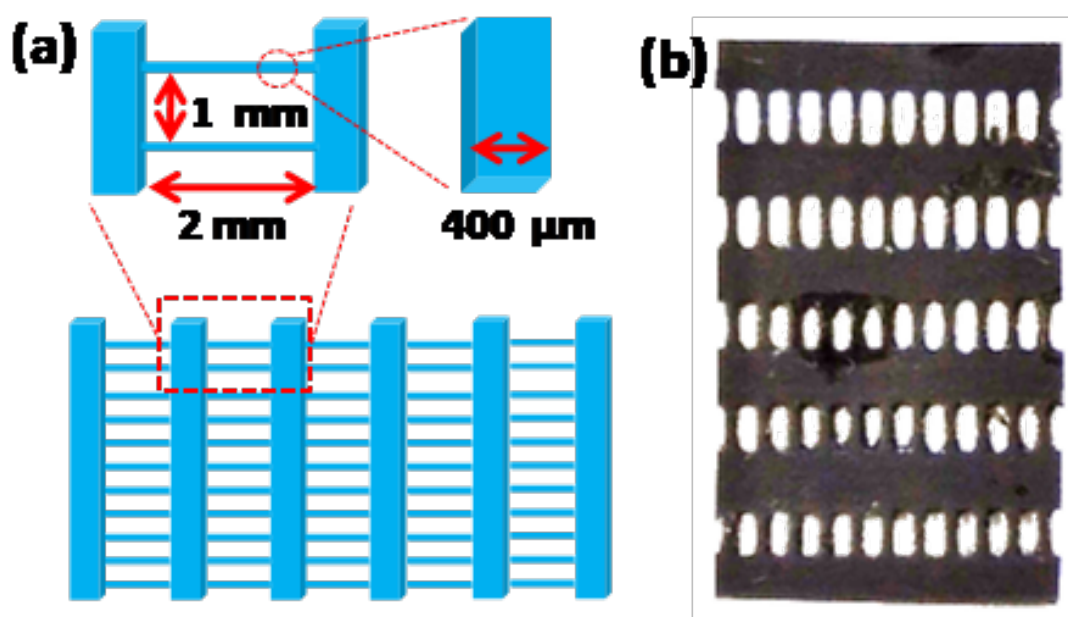


Figure 3.9. 3D printed array of sensor pads. (a) 3D design of the object. (b) 3D printed object.

3.3.3. Gas Sensing Setup. Shown in Figure 3.10 is a schematic of the experimental setup used for gas sensing measurements. For sensing operations, CuO/SWCNT was applied as a coat on a glass substrate and incorporated into the DC circuit, and encapsulated in a 2.5 L capacity steel chamber. The chamber consists of a heater with a PID controller to regulate the temperature. A specified amount of gas was injected into the sensing chamber with a fan for mixing to get the appropriate and stable gas concentration.

A simple electronic setup was used to determine the electrical resistance of the sensor. The electrical resistance is first converted to a DC voltage. A computer-aided Keithley source meter (model number 65487) with a six-digit display captured the PC's data using an RS-232 connection. The individual CuO/SWCNT gas sensor response

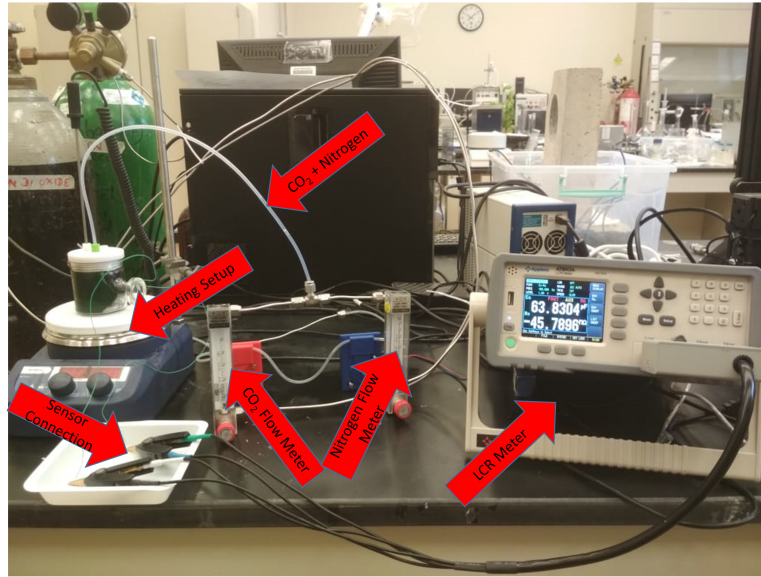


Figure 3.10. Photograph of gas sensor experimental set up

has been examined using Equation (3.1) [88, 89].

$$S(\%) = [(R_a - R_g)/R_a] \times 100 \quad (3.1)$$

where R_a is the resistance before and R_g is the resistance after the sample makes contact with gas at a constant temperature (27 °C). The sensors' electrical properties were measured using an LCR meter (inductance, capacitance, resistance) controlled by a PC that allowed automatic data acquisition. All the sensors prepared were measured in the same gas chamber under the same testing conditions. Capacitance is recorded for future data analysis.

3.4. Analysis

3.4.1. Gas Sensing. The sensors' electrical properties were measured using an LCR meter (inductance, capacitance, resistance) controlled by a PC that allowed automatic data acquisition. All the sensors prepared were measured in the same gas chamber under the same testing conditions. Capacitance was recorded for future data analysis.

3.4.2. Instruments for Measuring Properties. All the measurements were performed by a PerkinElmer TGA 4000 Thermogravimetric Analyzer in the range of 30–800 °C, with the rate of scanning 10 °C min⁻¹ under nitrogen condition. The Fourier transform infrared spectroscopy (FT-IR) was recorded using the PerkinElmer FTIR spectrometer Frontier using ZnSe crystal in the range of 500–4000 cm⁻¹. The scanning electron microscope (SEM) analysis was carried out using the JEOL JCM–6000 JCM–6000 Versatile Benchtop SEM instrument operated at an acceleration voltage of 5 and 30 kV to analyze the surface morphology of nanocomposite. The X-ray diffraction (XRD) was recorded using PANalytical EMPYREAN at 45 kV and 40 mA. All the equipment used is shown in Figure 3.11.

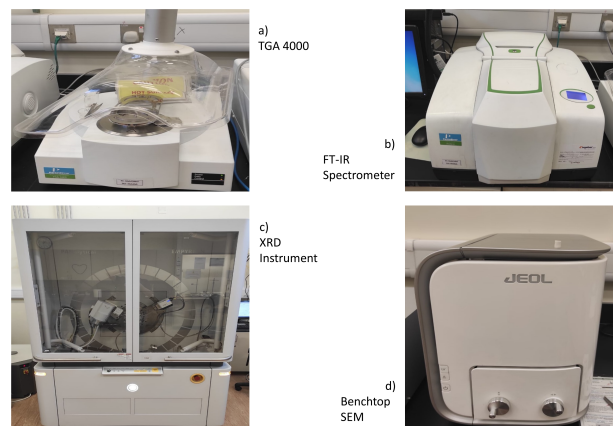


Figure 3.11. Showing the instruments used for characterization of the material

For electrical measurement, LCR meter from Applent AT810A with a 1 V voltage and 100 Hz frequency. The data points were saved each 600 ms and averaged over that time. The instrument is showing in Figure 3.12.

3.4.3. Design of Filtration pipe. Figure 3.13 shows the filtration pipe. Which will be fixed The use of an external turbine inlet fan alters the flow of air.the shown design is with a 80 degree twist.in a later chapter flow simulation will be done on many angles to decide on the right design.

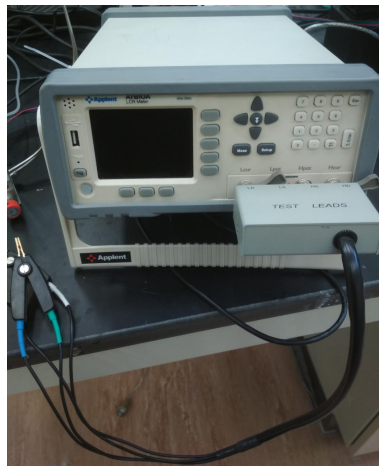


Figure 3.12. LCR meter used to obtain resistance values

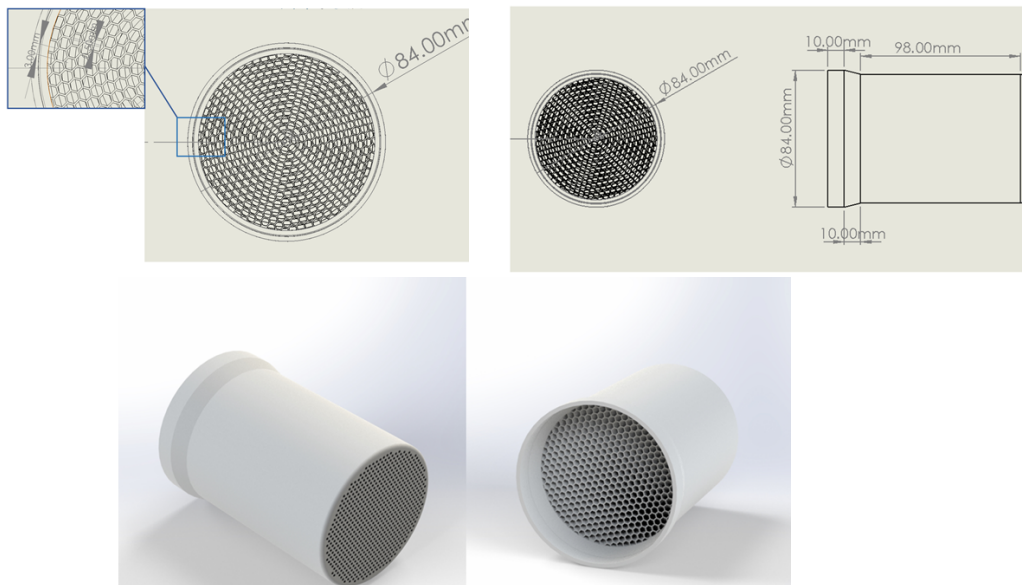


Figure 3.13. Shows the designed hexagonal filter.

3.4.4. Design of CO₂ Capturing Process. Capture and sequestration of CO₂ from power plants running on fossil fuels are vital strategies for halting global climate change. However, the commercially available technologies currently available such as scrubbing solvents, for example, aqueous amine solutions, are massive, exorbitantly costly, need a large amount of power within the context of power plants. Moreover,

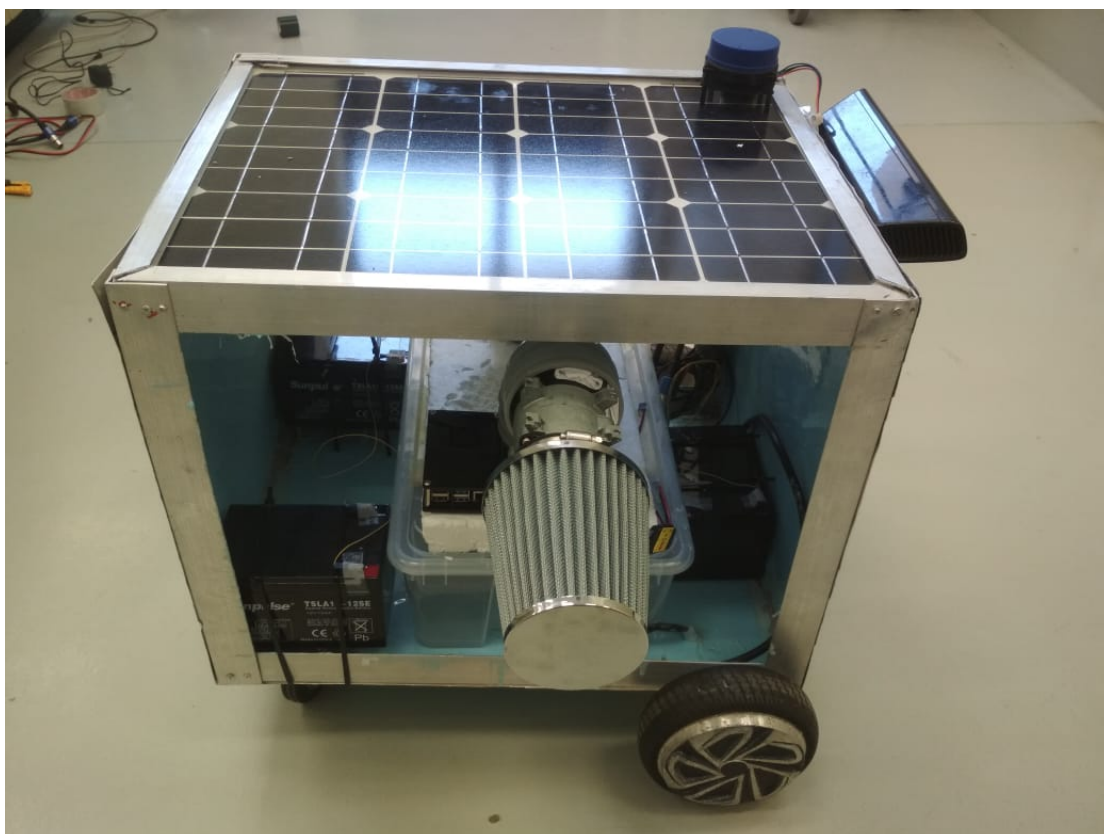


Figure 3.14. The vehicle that used to clean the environmental CO₂ and CO₂ release from industries using renewable energy

solvent towers may be more expensive, relatively speaking, for small scale capture at industries. Some innovative technologies may overcome these traditional limitations: membrane-based systems, metal-organic frameworks, solvent impregnated polymers, advanced CO₂ capture solvents, and micro-encapsulated solvents. Shifting the focus from conventional sorbents to novel sorbents with optimized geometries considering different parameters such as gas flow distribution, surface area per unit volume, pressure drop would result in much-reduced absorption towers. Those materials would gain from efficient mass transport that is reliant on reactor geometry. 3D printing has been revolutionary in many fields by allowing the fabrication of precisely controlled geometries. Direct ink writing is a layer-wise deposition technique in which shear-thinning inks are extruded through a nozzle into a specified pattern. This adaptive technology can print any ink with shear-thinning properties into complex geometries solidifying

the ink via temperature-induced phase change after extrusion, gelation, or evaporation. Functional structures have been made with this method, periodic graphene aerogels, organic metal frameworks, self-healing materials, wearable sensors, and microfluidics. This fabrication technology has also been used to build monoliths containing CO₂ capturing materials. This report demonstrates a CO₂ detection and removal method based on CuO/SWCNT nanocomposite and 3D printed sensors. Using these materials and sensors with an ROV will enable rapid detection and removal of CO₂ from indoors and possibly outdoors and potentially save lives and property

Chapter 4: Results and Discussion

4.1. Introduction

Gas sensors and challenges: The growth of automation and the internet of things resulted in a massive market for low energy sensors, which improved applicability in a wide range of materials. Such application includes manufacturing, health monitoring, smart cities, and even personalized health diagnostics. Nanostructured organic and inorganic materials have noticeably changed the field of gas sensing. The tunable surface, large specific surface, and good transport properties resulted in highly selective and sensitive gas sensing devices that are portable and have low energy consumption. The development of printed gas sensors and printing techniques resulted in growth among gas sensing materials. Materials such as metal oxides, conducting polymers, carbon nanotubes, and two-dimensional (2D) materials have improved due to printing techniques. Improvement of sensor performance is mostly obtained by working on materials design and device fabrication. Carbon dioxide CO₂ sensors used to monitor the Indoor Air Quality (IAQ) are a common requirement in buildings where ventilation takes place. Adapting the ventilation rates is needed to ensure the well-being of the occupants. Another use for CO₂ sensors is in cars and factories to monitor fumes emitted from these devices using either optical or chemical methods. Traditional sensors are based on metal oxides; solid-state electrodes usually require high operation temperature and have cross selectivity with other gasses. The use of polymer-based material is limited in the literature due to the limited sensitivity and selectivity and stable material for sensing. A sensor based on optical detection is accurate and fast in measurement; however, they are expensive and large.

4.2. Gas Sensing Properties of the 3D printed sensors

4.2.1. Characterization of the CNT/CuO/resin composite based 3D printed CO₂ sensor. The morphology and crystallinity of the fabricated sensor were characterized by SEM, XRD, TGA, and FTIR analysis. Figure 4.1 shows the SEM image of the 3D printed array of the sensor pad. From the SEM image, it is observed

that the array of sensing strips in the sensor pad is uniformly spaced and successfully printed per the CAD design. The zoomed-in image of the sensing stripes shows curved edges at the corners. The curved edges can be attributed to the excess composite curing at the corners during 3D printing, the CNT present in the composite acts as light scattering centers. At the sharp edges followed by hollow geometry, the scattering leads to excess resin curing, leading to the origin of curved edges during printing.

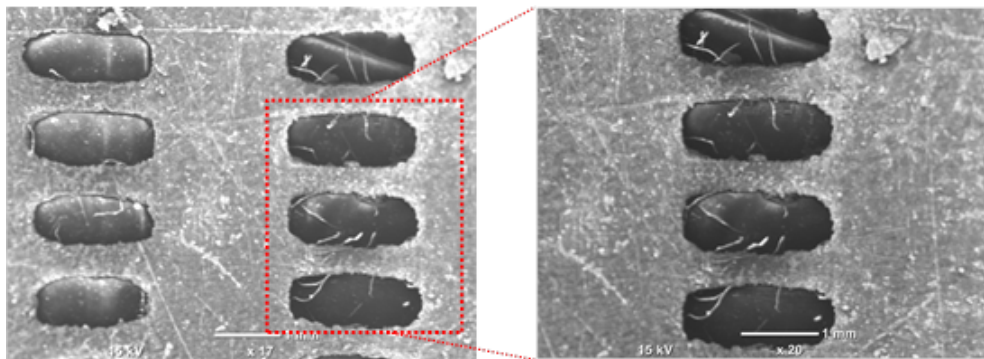


Figure 4.1. SEM images of the 3D printed sensor

Figure 4.2 shows the SEM images of the sensor pad, along with the measurement of the printed structure. Figure 4.2a shows that the calculated horizontal spacing between the array of sensors and the sensor strips' length comes out to be 1.95 mm and 1.92 mm, respectively. The printed strip's geometrical parameters are close to the 3D CAD design (2 mm) for printing. The magnified image of the sensor strips internal diameter is shown in Figure 4.2b. The thickness of the sensor strip is $402\ \mu\text{m}$ and interspacing between the strips is $705\ \mu\text{m}$, which is close to $400\ \mu\text{m}$ and $700\ \mu\text{m}$ as fed in the 3D CAD design. The slight variation in the thickness of the strips at the corners is due to excess curing of the composite by the light scattered through CNT embedded in the resin. The 3D printed sensor's close resemblance to the 3D design confirms the sensors' 3D printing parameters.

XRD has been used to determine the phase structure of the precursor that is obtained. XRD patterns of the CuO nanoparticles are shown in Figure 4.3. The scanning has been carried out from 4 to 100 by an increment of 0.02 and a scan speed

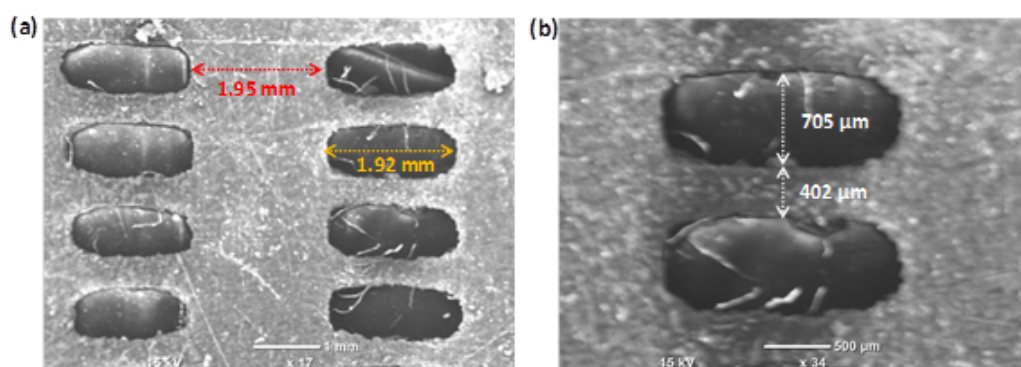


Figure 4.2. SEM images of the 3D printed sensor. (a) SEM image with calculated geometrical values in the horizontal direction. (b) SEM image with calculated geometrical values in the vertical direction

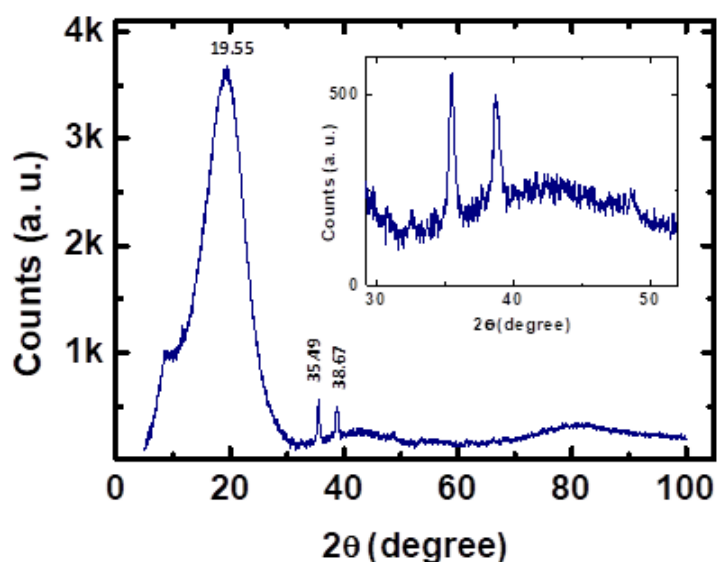


Figure 4.3. XRD plot of the 3D printed sensor. Inset shows the magnified image of the CuO peaks in the XRD plot

of 0.2s every step. The peaks 2θ of the as-synthesized CuO nanoparticles at 35.49 and 38.67 were indexed to the (111) and (111) planes. Inset shows the magnified image of the obtained CuO XDR peaks. The monoclinic structure of CuO of the samples is confirmed from these findings. The broadening of peaks indicated that the as-synthesized CuO nanoparticles are naturally polycrystalline. XRD patterns of the CuO nanoparticles are displayed.

4.2.2. Electrical Properties and Conductivity Measurements of The 3D Printed Sensor. The 3D printed sensor's electrical conductivity was measured by sequentially testing fabricated sensors having different %wt (0.05, 0.1, 0.15, 0.2, and 0.25) of CNT in the composite. The measurement was done by connecting the fabricated sensor with the LCR meter under an applied bias of 1V. The lower concentration of CNT in resin, i.e., 0.05 and 0.1 wt %, showed feeble conductivity, and resistance was in hundreds of mega ohms. With the increase in the CNT concentration, the increase in the conductivity is observed, and the calculated resistance of the 0.15 wt % composite was in hundreds of Kilo ohms. A similar increasing trend in conductivity was noticed for 0.2 wt % CNT, and the measured resistance was in tens of kilo ohm. With a further increase in the CNT wt% to 0.25%, the resistance was 100s micro ohms. This increase in conductivity with an increase in CNT concentration in the composite mixture can be explained based on the percolation theory. A detailed discussion of the theory-based percolation correlation between the conductive filler concentration and conductivity is discussed in the next section.

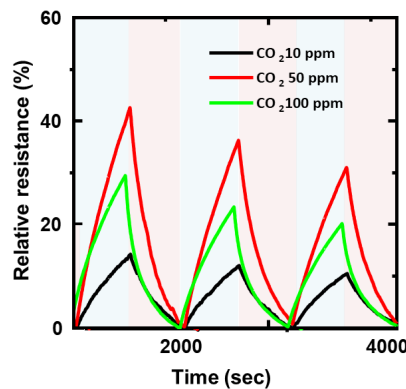


Figure 4.4. Shows continuous response of the composite 3d printed sensor to CO₂ at different concentration

Conductive polymer composites (CPCs) are defined as insulating polymer matrices that contain conductive fillers such as derivatives of carbon nanoscale structures or metallic particles, which can be zero, one, or even two-dimensional. An example would

be CNTs, graphene, or nanoscale particles of silver and gold. Percolation is defined as the sudden increase in thermoplastic polymer composites' conductivity at a filler's specific volume content. The percolation theory explains this phenomenon well and investigates the formation of conductive pathways, as shown in Figure 4.5 (c); the variation of the composites' electrical conductivity can be split into three different stages. The variation can be done by the gradual filling of some traditional conductive filler particles. In the first stage, the electrical conductivity is low as only a few carbon short fibers (CSFs) exist. The composites have similar conductivity to that of the polymer matrices. Nevertheless, it is essential to note that in Figure 4.5 (b), there is a formation of large clusters connected by CSFs. As there are CNTs close to each other, these composites' electrical conductivity increases gradually due to the tunneling effects. As explained later, this state is crucial for the change in nanocomposites' electrical resistivity. In the second stage, the number of CSFs increases, establishing the first complete electrically conductive path connected by some law. [Figure 4.5 (c), red path].

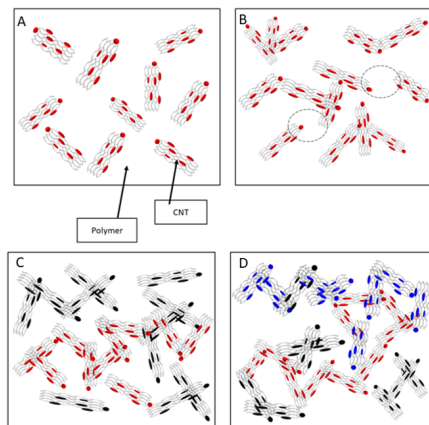


Figure 4.5. Schematic of the formation of conductive pathways in the polymer matrix according to percolation theory

Equation 4.1 based on percolation theory is given as below:

$$\sigma_c = \sigma_0(\phi_f - \phi_c)^t \quad (4.1)$$

where; ϕ_f The fraction of filler (v/v or wt. %);

σ_c is used to denote composite conductivity (S/cm);

σ_0 , filler electrical conductivity (S/cm);

σ_f , percolation threshold (v/v or wt %);

t, critical exponent as a fitting parameter.

The threshold value is calculated by plotting the conductivity of the composite versus reduced filler mass fraction and fitting the power-law function. Once the threshold is crossed, conductivity exponentially rises with an increase in the filler, and eventually, the saturation is reached.

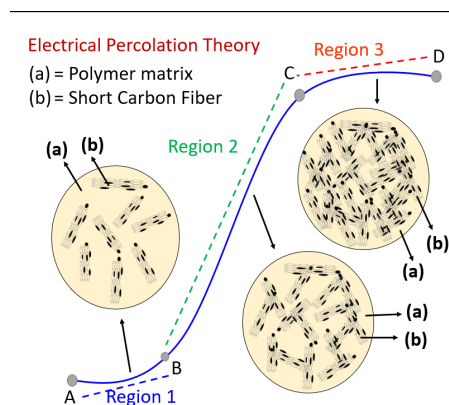


Figure 4.6. Schematic diagram showing the percolation behavior in polymer/conducting filler composites, point B onward (percolation threshold), point c onward (saturation level).

High aspect ratio fillers of length to diameter based on carbon allotropes (different structural forms), for example, carbon nanotubes compared to more traditional fillers like carbon black originate from their sheer size. While there is a significant development in melt blending, in situ polymerization, and solution mixing, the primary challenge remains to control nanocomposites' morphology. Particles' properties can be controlled to the required level once the morphology is modified. To print conductive structures such as electrodes and sensors with a 3D-printer, It is also important that the 3D printed polymers/CNT objects have significantly improved conductive properties matrix.

4.2.3. Semiconductor Analysis. The Keithley instrument was used to find the IV curve from -10 V to 10 V . It measures the current under constant temperature 22°C and relative humidity 40% shown in Figure 4.7.

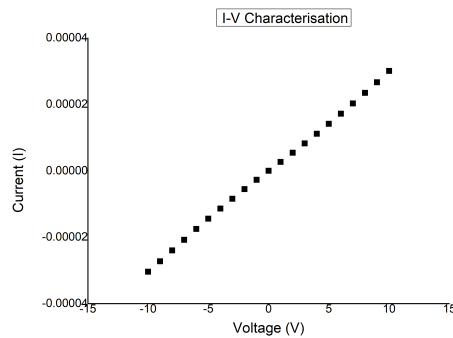


Figure 4.7. Showing the IV curve of the sensor

4.2.4. Sensitivity Analysis R_0 , is the sensor's resistance under N_2 or no gas exposure, and R is the resistance with gas exposure. The resistance changes when the target gas is released into the gas chamber. The sample was exposed to the CO_2 then the resistance of the sensor starts decreasing. As a result, a gradual increase in the relative resistance is observed throughout the 30 min exposure. On the other hand, when CO_2 gas feed was turned off, the resistance starts increasing, which is depicted with the decrease in the relative resistance, as shown in Figure 4.4. Within a 30 min window, the effect of CO_2 exposure is nullified, and the sensor reaches its initial resistance value. The sample was subjected to several CO_2 gas feed on-off cycles to confirm the sensor response's consistency. From Figure 4.8, it is clear that the fabricated sensor showed an almost similar response under a continuous on-off cycle of CO_2 exposure. The response was also checked by varying the CO_2 gas concentration in the test chamber from 101000 ppm. With an increase in the test gas concentration from 101000 ppm, an increase in the relative resistance is observed, as shown in Figure 4.8. These gas testing response results indicates that the fabricated sensor has sensitivity towards the CO_2 gas and even capable enough to detect the CO_2 gas at

low concentration. The response plot of the fabricated sensor was further analyzed to estimate the various parameters of the sensor. The nanocomposite response towards

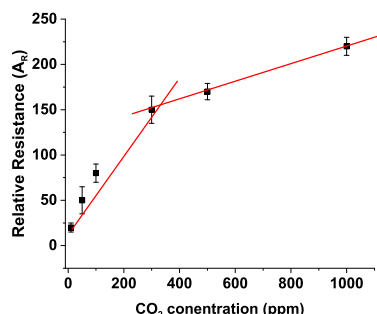


Figure 4.8. Figure shows a plot of the relative resistance vs CO₂ concentration.

CO₂ at different concentrations is shown in Figure 4.8 with concentrations of 10, 50, 100, 300, 500, and 1000 ppm. The resistance signal (response) from the sensor varies when exposed to different concentrations of CO₂. It can be observed that the nanocomposite shows significant response even at concentrations as low as 10 ppm level, with some visible differences around the baseline resistance at concentrations below 10 ppm. We can understand the limit of detection of the composite is 10 ppm. It shows good hysteresis at that concentration. The response time and recovery time are the sensor output time to reach 95% of the highest response. It can be noted from Figure that the response time is 2 min when the CO₂ gas is connected into the test chamber. Similarly, the resistance rises with a recovery time of 3 min when CO₂ gas is disconnected to the chamber.

4.2.5. FTIR. From the FTIR spectra, we can identify that the composite is showing peaks similar to the resin. So from the graph, it is evident that the resin composition is high in a composite when compared to CNT/CuO composition. In CNT, the carbons are sp^2 hybridized in a hexagonal lattice. All carbon is covalently bonded to neighboring carbons. Peak obtained in the range of 1580 cm^{-1} to 1530 cm^{-1} is the peak of sp^2 hybridized carbon. Peak obtained at 1200 cm^{-1} to 1100 cm^{-1} is the peak of sp^3 hybridized C=C. The C=O stretching vibrating bond is obtained

at the peak of 1800 to 1700. the peak obtained from 3000 to 2800 is the vibrational mode of C-H.

4.2.6. X-Ray Diffraction Patterns. X-ray diffraction patterns give the orientation patterns of the resin. By analyzing the graph, we can identify and calculate the

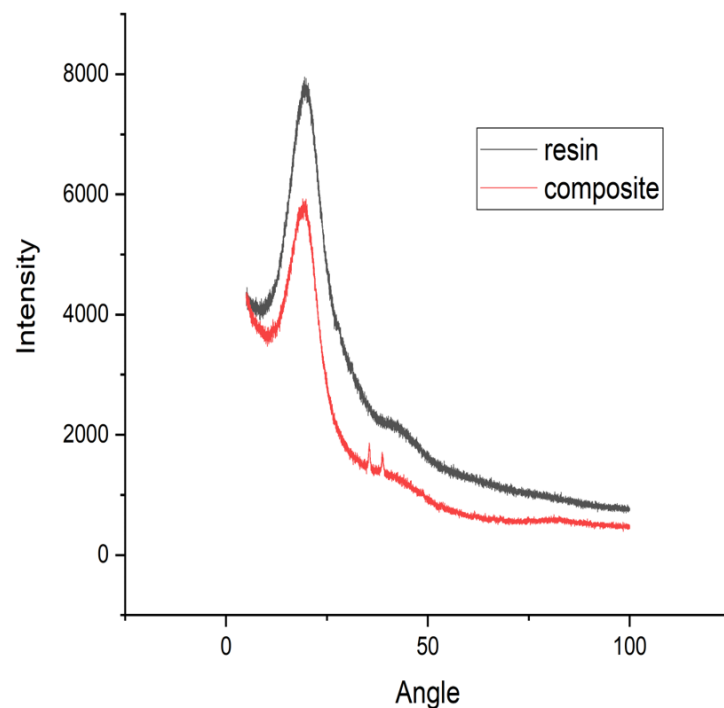


Figure 4.9. X-ray diffraction analysis for pure resin and composite material

d-spacing. The I_{max} value of the resin is obtained at two theta values 19.804. from the peak position, we can also identify that the lattice strain effect was uniform with no change in shape. In the case of composite, the I_{max} value is obtained at two theta values 19.03. The characteristic intense peak in resin and composite are mostly at the same angle. I_{max} value of resin is much higher than composite. On the addition of CNT/CuO in resin to make composite, the I_{max} peak to reduce to a lower intensity.

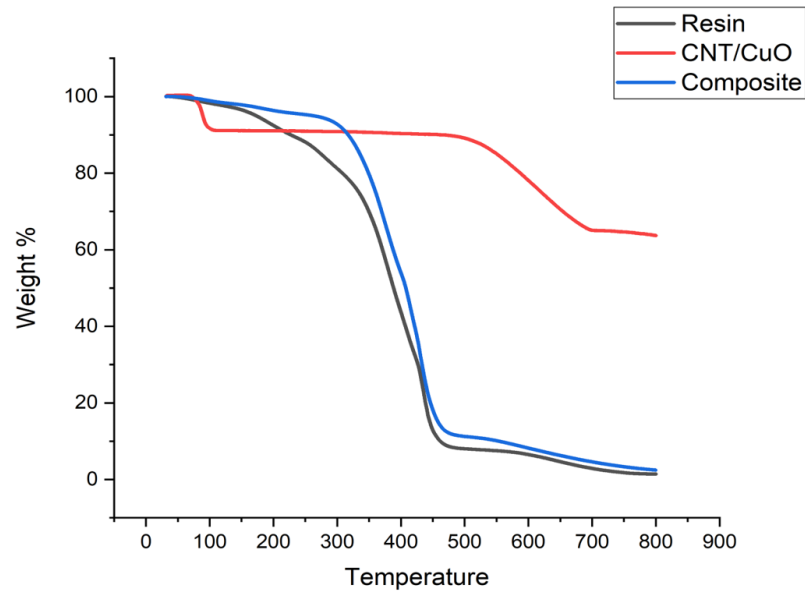


Figure 4.10. Showing TGA results of resin, filler, and composite

4.2.7. Thermogravimetric Analysis Results. TGA analysis is carried out to analyze the mass of the sample as the temperature changes. The TGA analysis is carried out from 25 °C to 800 °C. Oxidation of the composite started at 350 °C, and resin starts at 100 °C as for The oxidation of CNT/CuO started at 550 °C. The amount of resin composition in the composite is much higher compared to CNT/CuO composition. The fast oxidation of composite is due to the higher amount of resin, which reduces the heat transfer and decreases the oxidation rate.

4.3. Robotic Vehicle Results

4.3.1. E-Nose The E-nose is a collection of electrochemical sensors made from different metal-oxides. The main reason for using it is that most sensors are not selective to one gas but have different degrees of reaction to a specific gas. Thus, a collection of sensors is used to make a pattern response recognition software that can tell different gas compositions. This technology is not unique to electrochemical sensors but could be used with different technologies. An example would be potentiometric or amperometry or optical sensors, or a combination of all. The Figure 4.11

shows the sensor array that was made for MOX sensors. The details are in the performance chapter.

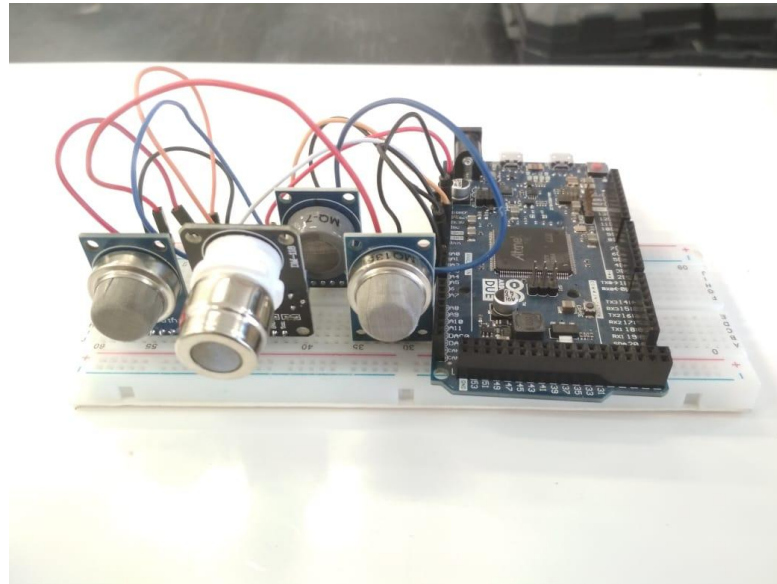


Figure 4.11. A sensor array is composed of different MOX sensors.

4.3.2. LiDAR Results LIDAR is a device for measuring distances by lighting up the target with a laser beam and measuring the reflected beam with a sensor. Differences in laser return times and wavelengths are used to make point-cloud representations of the target. In the presently reported prototype YDLIDAR X4 360-degree two-dimensional laser range scanner, LiDAR is used for real-time mapping. LiDARs are usually used for controlling the orientation and position of the robot. They can be used alone or combined with other sensors such as GPS and camera. Multiple sensors working together with useful algorithms can give better results. Combined with a camera and LiDAR, a mobile robot system can be deployed for mapping the local environment. The combination can allow mobile robots to locate and identify landmarks and correct their position and orientation automatically. This technique is called SLAM which is short for simultaneous localization and mapping. The device maps the surrounding based on the principle of triangulation distance measurement. Initially, the LiDAR starts rotating and scans in a clockwise direction on the request

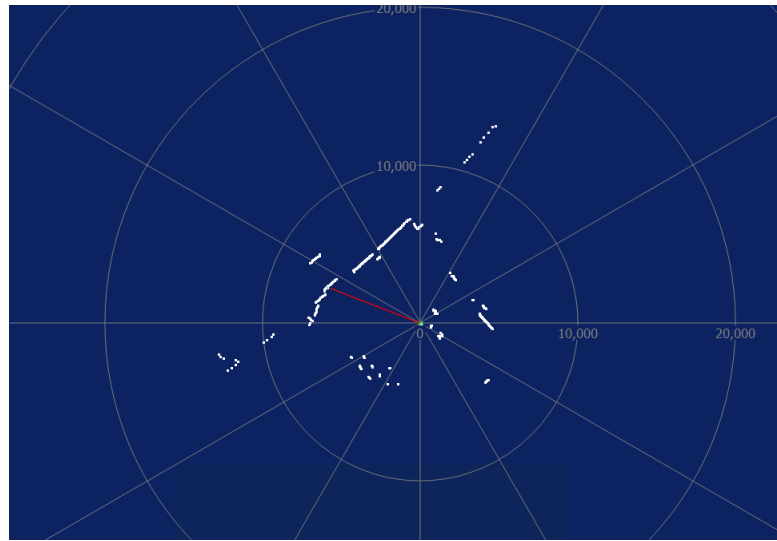


Figure 4.12. Showing LiDAR image of Hallway

for the mapping. Using the received optical signal as inputs and designed algorithms, the LiDAR generates a point-cloud map plot recorded through the communication interface. It receives spatial data from the laser scanner and constructs a 3D point cloud of an area during mapping. An experiment was conducted inside the entrance hall and other indoor locations to have a real testing environment. Figure 4.12 shows the real-time entrance hall environment's output data generated using the LiDAR assisted scanning approach. The developed 2D spatial map exhibits real-time roll/pitch that illustrates the scanned objects' trajectory and distance. The dots in the plot represent the number of people in the vicinity of the mapped area. By calculating the center's angular position and distance, the person's exact location can be estimated as represented by the red line in Figure 4.12. Thus the installed LiDAR in the current prototype assists the robot in mapping the area.

4.3.3. Depth Camera Results. The camera installed on the developed prototype is equipped with a unique microchip that generates a real-time three-dimensional picture of a nearby object. The area's condition can be ascertained. This 3D scanner system called Light Coding employs a variant of image-based 3D reconstruction. The device features an "RGB camera, depth sensor and microphone array running propri-

etary software," which provides full-body 3D motion capture, facial recognition, and voice recognition capabilities. The installed camera assists in interpreting the number of people stuck inside the area and their physical condition. Moreover, software technology enables advanced gesture recognition, facial recognition, and voice recognition to identify the person. The process of air/smoke filtration will help the camera get an overview of the location. Based on the inputs, if the situation looks under control, the robot will be guided to move to the next most affected location. Figure 4.13 shows a map obtained using a Kinect sensor as a proof of concept.

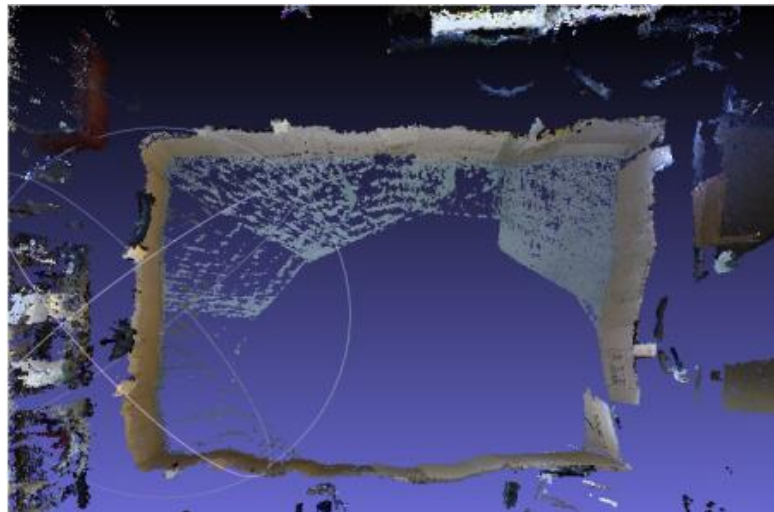
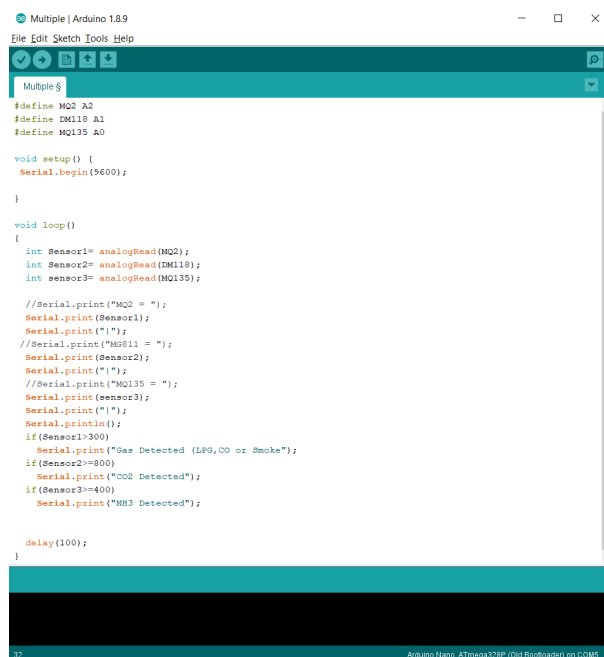


Figure 4.13. Showing a 3d map constructed from depth camera output [90]

4.3.4. Robot Vehicle Performance This thesis presents an effective coupling of novel techniques to build an automated system for detecting CO₂/smoke leakage and its effective capturing. The developed technology can be examined as an efficient integration of three innovative techniques. Firstly, the fabrication of CO₂ gas sensors via a 3D printing technique. The 3D printing approach enables the sensors' mass production quickly and controls the fabricated sensors' repeatability and sensitivity. The fabricated gas sensors installed at different buildings' location senses the leakage/emission of CO₂ gases. The gas sensor is developed by vat-polymerization based 3D printing technique, which is a relatively new technology. The 3D printing

techniques assisted fabrication of the gas sensor are best suited for the devices' economic bulk production and offer a high reproducibility rate. Secondly, a mobile robot is designed to wirelessly communicate with the fabricated CO₂ gas sensors and monitor the surrounding gas concentration. The robot's autonomous navigation is based on the inputs from fabricated CO₂ gas sensors installed in the building; a laser-based radar (LiDAR) that could assist in mapping of the building is reconstructed using algorithms. The LiDAR sensors installed on the robot assist. Overall, the fabricated gas sensor indicated an increase in the level of CO₂ in the surrounding. The robot gets the sensor data and identifies the installed sensor's location based on the robot's data during sensor installation in the building. Thus, the robot locates the sensor coordinates and locations, and the LiDAR system generates a navigation protocol using the software algorithm. Once the route is mapped, the robot tracks the path and drives the desired destination. Moreover, the camera installed on the robot gives the picture of the exact position of the affected region's whereabouts, like the number of persons stuck at the place, their condition through face and voice recognition technique. Thirdly, the other important aspect of the robot includes the CO₂ capturing technique embedded in the robot itself. In the pollutant capturing unit, the surface area, flow rate, and scaling of the unit's physical dimensions were optimized through simulation. The estimated designed capturing unit is proposed to be fabricated through 3D printing techniques using calcium chloride as a prime source for CO₂ absorption. The CO₂ capturing method relies on the filtration of the surrounding polluting air that is forced to pass through an absorption unit consisting of hexagonal channels. The design adopted for the filtration mechanism ensures bulk air treatment in a short time. Moreover, to further improve the absorption efficiency, the air is allowed to pass through a fluidic solution of calcium hydroxide placed inside the air purification chamber. Overall, the thesis's work successfully establishes a proof-of-concept platform that implements robot-assisted CO₂ monitoring and autonomous filtration technique. Moreover, the robot and algorithms are designed to operate in complex, real-world environments and gives scope to incorporate the technology for monitoring and filtration of other harmful gases like methane and carbon monoxide, and so on. The developed technology

has potential applications in all the buildings during fire accidents and in industries to locate gas leaks, identify hazardous areas with high concentration levels, and carry out necessary purification mechanisms. Figure 4.14 Arduino code is for reading analog results from 3 gas sensors: MQ2, DM118, and MQ135. First, gas sensors are connected to the Arduino Due. All Sensors need a preheat duration of about 30 seconds; after this preheat duration is finished, all sensors will produce analog output values. When MQ2 outputs value exceeding 300, LPG, CO, or Smoke gases will message the serial monitor that gas is detected; this process was done using if statements to compare the sensor output value with the minimum value to detect gas presence. For the DM118, this sensor will produce analog output in the presence of CO₂ gas, and once if the statement is true, the program will print CO₂ gas detected on the serial monitor. The MQ135 output value will exceed 400 in the presence of NH₃ gas, and the output message will be printed on the serial monitor that NH₃ gas is detected.



```

Multiple | Arduino 1.8.9
File Edit Sketch Tools Help

Multiple 9

#define MQ2 A2
#define DM118 A1
#define MQ135 A0

void setup() {
  Serial.begin(9600);
}

void loop()
{
  int sensor1= analogRead(MQ2);
  int sensor2= analogRead(DM118);
  int sensor3= analogRead(MQ135);

  //Serial.print("MQ2 = ");
  Serial.print(sensor1);
  Serial.print("\n");
  //Serial.print("MQ118 = ");
  Serial.print(sensor2);
  Serial.print("\n");
  //Serial.print("MQ135 = ");
  Serial.print(sensor3);
  Serial.print("\n");
  Serial.println();
  if(sensor1>300)
    Serial.print("Gas Detected (LPG,CO or Smoke)");
  if(sensor2==800)
    Serial.print("CO2 Detected");
  if(sensor3==400)
    Serial.print("NH3 Detected");

  delay(100);
}
32 Arduino Nano: ATmega328P (Old Bootloader) on COM5

```

Figure 4.14. Shows the Arduino code

4.3.5. CFD Analysis. A key aspects is to capture the carbon dioxide/smoke and purify the air during an emergency. For effective capture of the CO₂ and smoke

```

pythonProject pythonProject
pythonProject try1.py
1 import numpy as np
2 import matplotlib.pyplot as plt
3 import serial
4
5 plt.ion()
6 fig = plt.figure()
7 ser = serial.Serial('COM3', 9600)
8 ser.close()
9 ser.open()
10
11 i=0
12 x=list()
13 y1=list()
14 y2=list()
15 y3=list()
16 while True:
17     data = ser.readline().decode()
18     lineraw=data
19     S=lineraw.split(',')
20     MQ2=(int(S[0]))
21     DM118=(int(S[1]))
22     MQ135=(int(S[2]))
23     x.append(i)
24     y1.append(MQ2)
25     y2.append(DM118)
26     y3.append(MQ135)
27     plt.scatter(i,float(MQ2))
28     plt.scatter(i,float(DM118))
29     plt.scatter(i,float(MQ135))
30     i+=1
31     plt.show()
32     plt.pause(0.0001)

```

Figure 4.15. Shows the python code connecting the Arduino

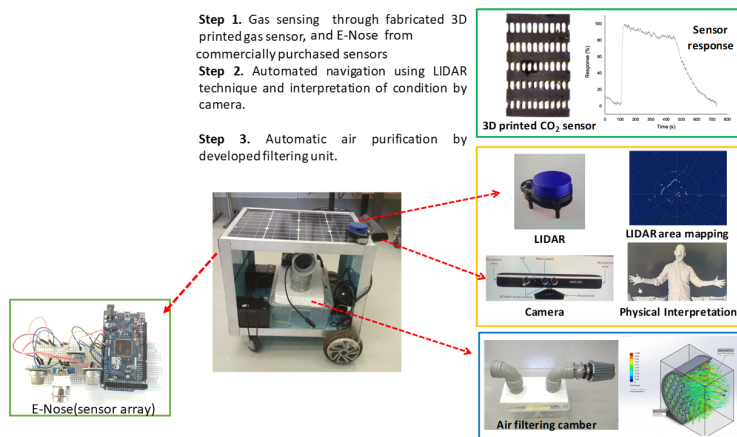


Figure 4.16. The overview of the robotic vehicle deployed for detection and capture of CO₂.

generated during fire accidents, it is desired to pass the contaminated air through pollutant absorbing channels. Inside the channels to maximize the CO₂ absorption, the channels' maximum surface area must be exposed to the polluted air. Thus, to have a design, a channeled unit with a maximum surface area that inter increase the absorption efficiency, a set of simulations were done, and results were analyzed. Compared to circular, square, and other geometry, the maximum hollow spatial fill density can be achieved by patterning the channeled hollow structure in a hexagonal arrangement.; simulations were done by considering the hexagonal channeled structure with different twist angles. To have a wide variety of testing conditions. Overall, the simulation's objective is to get the optimum design for the capturing unit that offers maximum surface exposure without affecting the channels' airflow rate. Figure 4.17 shows the simulation results for the airflow within hexagonal channels having different twist angles. The flow rate variation inside the channels is mapped with a color-coding represented as a scale bar on the left Figure. Compared to the other designed channels, the hexagonal arrangement having a twist angle of 80% offers the highest flow rate within the channels, i.e., 10 m/s. Even the average flow rate inside the channels with an 80% twist angle is 6 m/s, which is better than the other designed channels. Thus from the simulation results, it can be inferred that the 80% twist angle hexagonal channels offer the highest flow rate. The estimated results of the other vital parameters of the designed units like surface area and pressure drop are listed in Table 4.1. From the examined parameter shown in Table 4.1, it is established that compared to other designs the hexagonal channel with a twist angle of 80% offers maximum surface exposure and pressure drop. As a result, the simulation analysis reveals that the hexagonal channels with an 80% twist angle are best suited for fabricated an effective CO₂/smoke capturing unit.

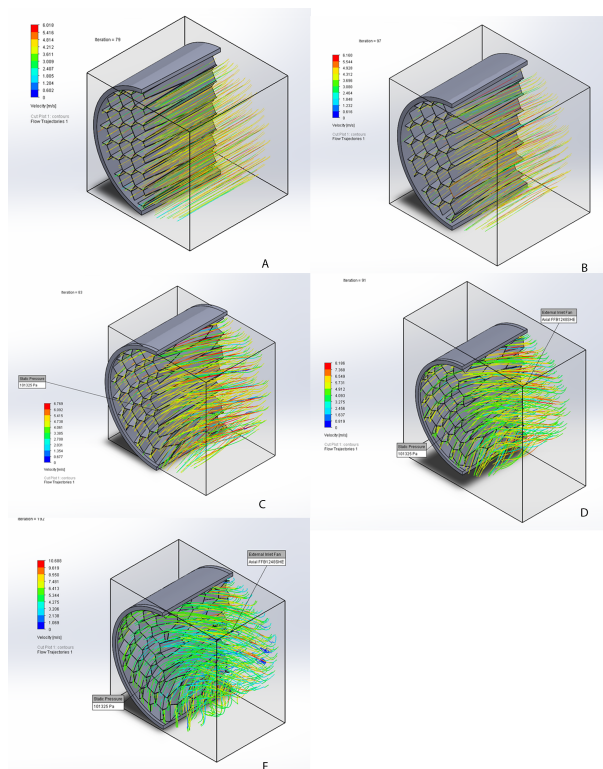


Figure 4.17. Flowchart showing simulation results for different twist angles

Table 4.1. Showing a table summarizing the simulation results

Twist angle	volume cubic mil- limeters	Surface area increase	Pressure drop
0deg	1941245.9	0.0	5.83
10deg	1941270	0.2	10.43
30deg	1941323.63	1.9	19.96
50deg	1941247.45	5.0	22.53
80deg	1941252.01	12.1	27.86

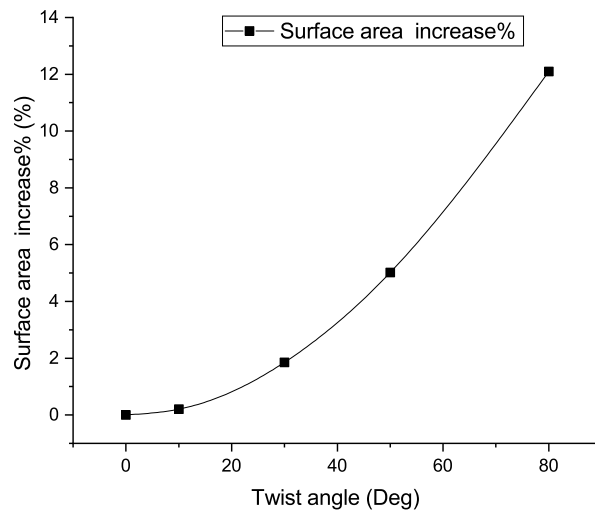


Figure 4.18. Showing surface increase with twist angle

Chapter 5: Conclusion

Mobile robotics-assisted harmful gas monitoring and air purification are part of a multidisciplinary research field that tackles the challenge of combining gas sensing and air purification technologies into a mobile robot. Developing these type of systems for real-world applications requires tackling issues related to gas dispersion. In this thesis, we focused on gas concentration monitoring enabling autonomous air purification of the affected region intended for practical applications. The approach included a 3D printed gas sensor for monitoring the CO₂ and an e-nose fabricated using commercially available sensors such as NH₃, LPG, and CO. A robot equipped with the air filtration mechanism and algorithm to establish communication between the sensor and the filtration system. CO₂ sensor for monitoring gas sensor was fabricated successfully by 3D printing as set out in one of the objectives. The 3D printing approach establishes the reproducible, repeatable, and cost-effective method for the sensor's bulk production. The fabricated sensor can detect CO₂ concentrations of different levels and has high selectivity towards CO₂ gas. In the next phase, a mobile robot embedded with the air filtration module was integrated . The fast air and effective filtration were achieved by incorporating a novel filter design and filtration mechanism. Soon, we believe the possibility of using this kind of prototype as a vehicles that can move towards the CO₂ polluted areas upon getting the alarming signals from various sensors kept in different local environments.

References

- [1] "Exposure to Smoke from Fires." [Online]. Available: www.health.ny.gov/environmental/outdoors/air/smoke_from_fire.htm
- [2] Y. Xu, X. Wu, X. Guo, B. Kong, M. Zhang, X. Qian, S. Mi, and W. Sun, "The Boom in 3D-Printed Sensor Technology," *Sensors*, vol. 17, no. 5, p. 1166, may 2017. [Online]. Available: <http://www.mdpi.com/1424-8220/17/5/1166>
- [3] P. Puligundla, J. Jung, and S. Ko, "Carbon dioxide sensors for intelligent food packaging applications," pp. 328–333, may 2012.
- [4] P. ZHANG, H. QIN, H. ZHANG, W. LÜ, and J. HU, "CO₂ gas sensors based on Yb_{1-x}CaxFeO₃ nanocrystalline powders," *J. Rare Earths*, vol. 35, no. 6, pp. 602–609, 2017.
- [5] A. Ghosh, C. Zhang, S. Shi, and H. Zhang, "High temperature CO₂ sensing and its cross-sensitivity towards H₂ and CO gas using calcium doped ZnO thin film coated langasite SAW sensor," *Sensors Actuators, B Chem.*, vol. 301, no. August, p. 126958, 2019. [Online]. Available: <https://doi.org/10.1016/j.snb.2019.126958>
- [6] M. Habib, S. S. Hussain, S. Riaz, and S. Naseem, "Preparation and characterization of zno nanowires and their applications in co₂ gas sensors," *Materials Today: Proceedings*, vol. 2, no. 10, pp. 5714–5719, 2015.
- [7] A. I. Daud, K. Wahid, and W. M. Khairul, "Room-temperature operated cyano-terminated ethynylated-thiourea as a resistive-type carbon dioxide (co₂) gas sensor," *Organic Electronics*, vol. 70, pp. 32–41, 2019.
- [8] A. Ghosh, C. Zhang, S. Shi, and H. Zhang, "High temperature co₂ sensing and its cross-sensitivity towards h₂ and co gas using calcium doped zno thin film coated langasite saw sensor," *Sensors and Actuators B: Chemical*, vol. 301, p. 126958, 2019.

- [9] Z. Ahmad, S. Manzoor, M. Talib, S. Islam, P. Mishra *et al.*, "Self-standing mwcnts based gas sensor for detection of environmental limit of co₂," *Materials Science and Engineering: B*, vol. 255, p. 114528, 2020.
- [10] B. Sun, G. Xie, Y. Jiang, and X. Li, "Comparative co₂-sensing characteristic studies of pei and pei/starch thin film sensors," *Energy Procedia*, vol. 12, pp. 726–732, 2011.
- [11] T. Bräunl, *Embedded robotics: mobile robot design and applications with embedded systems*. Springer Science & Business Media, 2008.
- [12] Linorobot, "Linorobot: ROS Compatible ground robots (2WD, 4WD, Ackermann Steering, Mecanum Drive)." [Online]. Available: <https://github.com/linorobot/linorobot>
- [13] G. A. Terejanu *et al.*, "Extended kalman filter tutorial," *University at Buffalo*, 2008.
- [14] Nasa-jpl, "open-source-rover: A build-it-yourself, 6-wheel rover based on the rovers on Mars!" [Online]. Available: <https://github.com/nasa-jpl/open-source-rover>
- [15] M. Asad, O. Al Aidaros, R. Beg, M. Al Dhahri, S. Al Neyadi, and M. Hussein, "Development of autonomous drone for gas sensing application," in *2017 International Conference on Electrical and Computing Technologies and Applications (ICECTA)*. IEEE, 2017, pp. 1–6.
- [16] P. P. Neumann, S. Asadi, A. J. Lilienthal, M. Bartholmai, and J. H. Schiller, "Autonomous gas-sensitive microdrone: Wind vector estimation and gas distribution mapping," *IEEE robotics & automation magazine*, vol. 19, no. 1, pp. 50–61, 2012.
- [17] PTI, "Novel CO₂ capturing tech may cut vehicle emissions by 90%," 2019. [Online]. Available: <https://auto.economictimes.indiatimes.com/news/auto-technology/novel-co2-capturing-tech-may-cut-vehicle-emissions-by-90/72962390>

- [18] A. Tarantola, "These robotic 'trees' can turn CO₂ into concrete," 2018. [Online]. Available: <https://www.engadget.com/2018-09-11-robot-trees-co2-into-concrete-climate-change.html>
- [19] P. Patel, "Carbon capture just got cheaper and more efficient," *Anthr. Mag.*, 2019. [Online]. Available: <https://www.anthropocenemagazine.org/2019/10/battery-like-device-could-capture-carbon-dioxide-from-air-and-exhaust-pipes/>
- [20] UKEssays, "The Robot Tree A New Ecofriendly Technology Environmental Sciences Essay," 2018. [Online]. Available: <https://www.ukessays.com/essays/environmental-sciences/the-robot-tree-a-new-ecofriendly-technology-environmental-sciences-essay.php?vref=1>
- [21] U. K. Kim, H. N. CHANG, M. H. Lee, and H. S. Park, "Movable air purification robot system," 2010. [Online]. Available: <https://patents.google.com/patent/US8496737>
- [22] A. Gebhardt, "Understanding additive manufacturing," 2011.
- [23] K. Deshmukh, M. T. Houkan, M. A. AlMaadeed, and K. K. Sadasivuni, "Introduction to 3d and 4d printing technology: State of the art and recent trends," in *3D 4D Print. Polym. Nanocomposite Mater.* Elsevier, 2020, pp. 1–24. [Online]. Available: <https://linkinghub.elsevier.com/retrieve/pii/B9780128168059000016>
- [24] A. Ambrosi and M. Pumera, "3D-printing technologies for electrochemical applications," *Chem. Soc. Rev.*, vol. 45, no. 10, pp. 2740–2755, 2016. [Online]. Available: <http://xlink.rsc.org/?DOI=C5CS00714C>
- [25] M. Mrlik, P. Sobolciak, I. Krupa, and P. Kasak, "Light-controllable viscoelastic properties of a photolabile carboxybetaine ester-based polymer with mucus and cellulose sulfate," *Emergent Mater.*, vol. 1, no. 1-2, pp. 35–45, jun 2018. [Online]. Available: <http://link.springer.com/10.1007/s42247-018-0004-2>
- [26] D. Ponnamma, A. Erturk, H. Parangusan, K. Deshmukh, M. B. Ahamed, and M. Al Ali Al-Maadeed, "Stretchable quaternary phasic PVDF-HFP

- nanocomposite films containing graphene-titania-SrTiO₃ for mechanical energy harvesting," *Emergent Mater.*, vol. 1, no. 1-2, pp. 55–65, jun 2018. [Online]. Available: <http://link.springer.com/10.1007/s42247-018-0007-z>
- [27] T. Meng, C. Yi, L. Liu, A. Karim, and X. Gong, "Enhanced thermoelectric properties of two-dimensional conjugated polymers," *Emergent Mater.*, vol. 1, no. 1-2, pp. 67–76, jun 2018. [Online]. Available: <http://link.springer.com/10.1007/s42247-018-0002-4>
- [28] A. Nagaraj, D. Govindaraj, and M. Rajan, "Magnesium oxide entrapped Polypyrrole hybrid nanocomposite as an efficient selective scavenger for fluoride ion in drinking water," *Emergent Mater.*, vol. 1, no. 1-2, pp. 25–33, jun 2018. [Online]. Available: <http://link.springer.com/10.1007/s42247-018-0001-5>
- [29] A. Muzaffar, M. B. Ahamed, K. Deshmukh, and J. Thirumalai, "A review on recent advances in hybrid supercapacitors: Design, fabrication and applications," *Renew. Sustain. Energy Rev.*, vol. 101, pp. 123–145, mar 2019. [Online]. Available: <https://linkinghub.elsevier.com/retrieve/pii/S1364032118307299>
- [30] G. Chisholm, P. J. Kitson, N. D. Kirkaldy, L. G. Bloor, and L. Cronin, "3D printed flow plates for the electrolysis of water: an economic and adaptable approach to device manufacture," *Energy Environ. Sci.*, vol. 7, no. 9, pp. 3026–3032, 2014. [Online]. Available: <http://xlink.rsc.org/?DOI=C4EE01426J>
- [31] K. K. Sadasivuni, S. Rattan, K. Deshmukh, A. Muzaffar, M. B. Ahamed, S. K. K. Pasha, P. Mazumdar, S. Waseem, Y. Grohens, and B. Kumar, "Chapter 12. hybrid nano-filler for value added rubber compounds for recycling," 2018, pp. 310–329. [Online]. Available: <http://ebook.rsc.org/?DOI=10.1039/9781788013482-00310>
- [32] X. Wei, D. Li, W. Jiang, Z. Gu, X. Wang, Z. Zhang, and Z. Sun, "3D Printable Graphene Composite," *Sci. Rep.*, vol. 5, no. 1, p. 11181, sep 2015. [Online]. Available: <http://www.nature.com/articles/srep11181>
- [33] S. Sankaran, K. Deshmukh, M. B. Ahamed, S. K. K. Pasha, K. K. Sadasivuni, D. Ponnamma, M. A.-A. AlMaadeed, and K. Chidambaram,

- “Investigation on the Electrical Properties of Lithium Ion Conducting Polymer Electrolyte Films Based on Biodegradable Polymer Blends,” *Adv. Sci. Lett.*, vol. 24, no. 8, pp. 5496–5502, aug 2018. [Online]. Available: <https://www.ingentaconnect.com/content/10.1166/asl.2018.12136>
- [34] A. H. Loo, C. K. Chua, and M. Pumera, “DNA biosensing with 3D printing technology,” *Analyst*, vol. 142, no. 2, pp. 279–283, 2017. [Online]. Available: <http://xlink.rsc.org/?DOI=C6AN02038K>
- [35] T.-t. QIAN, D. LIU, X.-j. TIAN, C.-m. LIU, and H.-m. WANG, “Microstructure of TA2/TA15 graded structural material by laser additive manufacturing process,” *Trans. Nonferrous Met. Soc. China*, vol. 24, no. 9, pp. 2729–2736, sep 2014. [Online]. Available: <https://linkinghub.elsevier.com/retrieve/pii/S100363261463404X>
- [36] U. G. K. Wegst, H. Bai, E. Saiz, A. P. Tomsia, and R. O. Ritchie, “Bioinspired structural materials,” *Nat. Mater.*, vol. 14, no. 1, pp. 23–36, jan 2015. [Online]. Available: <http://www.nature.com/articles/nmat4089>
- [37] C. Zhu, T. Y.-J. Han, E. B. Duoss, A. M. Golobic, J. D. Kuntz, C. M. Spadaccini, and M. A. Worsley, “Highly compressible 3d periodic graphene aerogel microlattices,” *Nature communications*, vol. 6, no. 1, pp. 1–8, 2015.
- [38] S. Sankaran, K. Deshmukh, M. B. Ahamed, and S. Khadheer Pasha, “Recent advances in electromagnetic interference shielding properties of metal and carbon filler reinforced flexible polymer composites: A review,” *Compos. Part A Appl. Sci. Manuf.*, vol. 114, pp. 49–71, nov 2018. [Online]. Available: <https://linkinghub.elsevier.com/retrieve/pii/S1359835X18303130>
- [39] M. R. Cutkosky and S. Kim, “Design and fabrication of multi-material structures for bioinspired robots,” *Philos. Trans. R. Soc. A Math. Phys. Eng. Sci.*, vol. 367, no. 1894, pp. 1799–1813, may 2009. [Online]. Available: <https://royalsocietypublishing.org/doi/10.1098/rsta.2009.0013>

- [40] G. Gentile, F. Greco, and D. Larobina, "Stress-relaxation behavior of a physical gel: Evidence of co-occurrence of structural relaxation and water diffusion in ionic alginate gels," *Eur. Polym. J.*, vol. 49, no. 12, pp. 3929–3936, dec 2013. [Online]. Available: <https://linkinghub.elsevier.com/retrieve/pii/S0014305713004382>
- [41] G. J. Thangamani, K. Deshmukh, K. Chidambaram, M. B. Ahamed, K. K. Sadasivuni, D. Ponnamma, M. Faisal, N. A. Nambiraj, and S. K. K. Pasha, "Influence of CuO nanoparticles and graphene nanoplatelets on the sensing behaviour of poly(vinyl alcohol) nanocomposites for the detection of ethanol and propanol vapors," *J. Mater. Sci. Mater. Electron.*, vol. 29, no. 6, pp. 5186–5205, mar 2018. [Online]. Available: <http://link.springer.com/10.1007/s10854-017-8484-z>
- [42] D. J. Beebe, J. S. Moore, J. M. Bauer, Q. Yu, R. H. Liu, C. Devadoss, and B.-H. Jo, "Functional hydrogel structures for autonomous flow control inside microfluidic channels," *Nature*, vol. 404, no. 6778, pp. 588–590, apr 2000. [Online]. Available: <http://www.nature.com/articles/35007047>
- [43] D. Ponnamma, M. M. Chamakh, K. Deshmukh, M. Basheer Ahamed, A. Erturk, P. Sharma, and M. A.-A. Al-Maadeed, "Ceramic-based polymer nanocomposites as piezoelectric materials," 2017, pp. 77–93. [Online]. Available: http://link.springer.com/10.1007/978-3-319-50424-7{ }_3
- [44] A. Muzaffar, M. B. Ahamed, K. Deshmukh, M. Faisal, and S. K. Pasha, "Enhanced electromagnetic absorption in NiO and BaTiO₃ based polyvinylidene fluoride nanocomposites," *Mater. Lett.*, vol. 218, pp. 217–220, may 2018. [Online]. Available: <https://linkinghub.elsevier.com/retrieve/pii/S0167577X18302258>
- [45] C. Lin, J. Lin, and T. Ko, "Optimisation of the EDM Process Based on the Orthogonal Array with Fuzzy Logic and Grey Relational Analysis Method," *Int. J. Adv. Manuf. Technol.*, vol. 19, no. 4, pp. 271–277, feb 2002. [Online]. Available: <http://link.springer.com/10.1007/s001700200034>

- [46] K. Deshmukh, M. B. Ahamed, R. R. Deshmukh, K. K. Sadasivuni, D. Ponnamma, S. K. K. Pasha, M. A.-A. AIMaadeed, A. R. Polu, and K. Chidambaram, "Eeonomer 200F®: A High-Performance Nanofiller for Polymer Reinforcement Investigation of the Structure, Morphology and Dielectric Properties of Polyvinyl Alcohol/Eeonomer-200F® Nanocomposites for Embedded Capacitor Applications," *J. Electron. Mater.*, vol. 46, no. 4, pp. 2406–2418, apr 2017. [Online]. Available: <http://link.springer.com/10.1007/s11664-017-5304-4>
- [47] Q. Ge, C. K. Dunn, H. J. Qi, and M. L. Dunn, "Active origami by 4D printing," *Smart Mater. Struct.*, vol. 23, no. 9, p. 094007, sep 2014. [Online]. Available: <https://iopscience.iop.org/article/10.1088/0964-1726/23/9/094007>
- [48] M. Singh, H. M. Haverinen, P. Dhagat, and G. E. Jabbour, "Inkjet Printing-Process and Its Applications," *Adv. Mater.*, vol. 22, no. 6, pp. 673–685, feb 2010. [Online]. Available: <http://doi.wiley.com/10.1002/adma.200901141>
- [49] A. Bhatnagar, W. Hogland, M. Marques, and M. Sillanpää, "An overview of the modification methods of activated carbon for its water treatment applications," 2013.
- [50] K. Kaneko, C. Ishii, M. Ruike, and H. Kuwabara, "Origin of superhigh surface area and microcrystalline graphitic structures of activated carbons," *Carbon N. Y.*, 1992.
- [51] W. Li, K. Yang, J. Peng, L. Zhang, S. Guo, and H. Xia, "Effects of carbonization temperatures on characteristics of porosity in coconut shell chars and activated carbons derived from carbonized coconut shell chars," *Ind. Crops Prod.*, 2008.
- [52] M. Tadda, A. Ahsan, A. Shitu, M. ElSergany, T. Arunkumar, B. Jose, M. A. Razzaque, and N. N. Daud, "A review on activated carbon: process, application and prospects," *Journal of Advanced Civil Engineering Practice and Research*, vol. 2, no. 1, pp. 7–13, 2016.

- [53] H. S. Min, M. Abbas, R. Kanthasamy, H. Abdul Aziz, and C. C. Tay, "Activated carbon: prepared from various precursors," *Ideal Int. E-publication Pvt. Ltd*, pp. 1–20, 2017.
- [54] B. K. Pradhan and N. K. Sandle, "Effect of different oxidizing agent treatments on the surface properties of activated carbons," *Carbon N. Y.*, 1999.
- [55] A. Barroso-Bogeat, M. Alexandre-Franco, C. Fernandez-Gonzalez, and V. Gomez-Serrano, "Activated carbon surface chemistry: Changes upon impregnation with al (iii), fe (iii) and zn (ii)-metal oxide catalyst precursors from no₃- aqueous solutions," *Arabian Journal of Chemistry*, vol. 12, no. 8, pp. 3963–3976, 2019.
- [56] H. Marsh and F. Rodriguez-Reinoso, "Activation Processes (Chemical)," in *Act. Carbon*. Elsevier, 2006, pp. 322–365. [Online]. Available: <https://linkinghub.elsevier.com/retrieve/pii/B9780080444635500200>
- [57] —, "Activation Processes (Thermal or Physical)," in *Act. Carbon*. Elsevier, 2006, pp. 243–321. [Online]. Available: <https://linkinghub.elsevier.com/retrieve/pii/B9780080444635500194>
- [58] A. Veksha, T. I. Bhuiyan, and J. M. Hill, "Activation of aspen wood with carbon dioxide and phosphoric acid for removal of total organic carbon from oil sands produced water: Increasing the yield with bio-oil recycling," *Materials*, vol. 9, no. 1, p. 20, 2016.
- [59] F. Rodriguez-Reinoso, M. Molina-Sabio, and M. González, "The use of steam and co₂ as activating agents in the preparation of activated carbons," *Carbon*, vol. 33, no. 1, pp. 15–23, 1995.
- [60] K. Chue, J. Kim, Y. Yoo, S. Cho, and R. Yang, "Comparison of activated carbon and zeolite 13x for co₂ recovery from flue gas by pressure swing adsorption," *Industrial & Engineering Chemistry Research*, vol. 34, no. 2, pp. 591–598, 1995.
- [61] G. Li, P. Xiao, P. Webley, J. Zhang, R. Singh, and M. Marshall, "Capture of co₂ from high humidity flue gas by vacuum swing adsorption with zeolite 13x," *Adsorption*, vol. 14, no. 2-3, pp. 415–422, 2008.

- [62] M. Zarghampoor, M. Mozaffarian, M. Soleimani, and M. T. Ravanchi, "Modeling of co₂ adsorption on activated carbon and 13x zeolite via vacuum swing adsorption," in *IOP Conference Series: Materials Science and Engineering*, vol. 206, 2017.
- [63] L. Ma, J. Li, and X. Ma, "Preparation and adsorption of co₂ and h₂ by activated carbon hollow fibers from rubber wood (*hevea brasiliensis*)," *BioResources*, vol. 14, no. 4, pp. 9755–9765, 2019.
- [64] G.-g. Huang, Y.-f. Liu, X.-x. Wu, and J.-j. Cai, "Activated carbons prepared by the koh activation of a hydrochar from garlic peel and their co₂ adsorption performance," *New Carbon Materials*, vol. 34, no. 3, pp. 247–257, 2019.
- [65] J. Sreńscek-Nazzal and K. Kiełbasa, "Advances in modification of commercial activated carbon for enhancement of co₂ capture," *Applied Surface Science*, vol. 494, pp. 137–151, 2019.
- [66] Y. Guo, C. Tan, J. Sun, W. Li, J. Zhang, and C. Zhao, "Porous activated carbons derived from waste sugarcane bagasse for co₂ adsorption," *Chemical Engineering Journal*, vol. 381, p. 122736, 2020.
- [67] D. Li, J. Zhou, Y. Wang, Y. Tian, L. Wei, Z. Zhang, Y. Qiao, and J. Li, "Effects of activation temperature on densities and volumetric co₂ adsorption performance of alkali-activated carbons," *Fuel*, vol. 238, pp. 232–239, 2019.
- [68] S. Rattanaphan, T. Rungrotmongkol, and P. Kongsune, "Biogas improving by adsorption of co₂ on modified waste tea activated carbon," *Renewable Energy*, vol. 145, pp. 622–631, 2020.
- [69] F. Lou, A. Zhang, G. Zhang, L. Ren, X. Guo, and C. Song, "Enhanced kinetics for co₂ sorption in amine-functionalized mesoporous silica nanosphere with inverted cone-shaped pore structure," *Applied Energy*, vol. 264, p. 114637, 2020.
- [70] P. Zhao, G. Zhang, Y. Xu, and Y. Lv, "Amine functionalized hierarchical bimodal mesoporous silicas as a promising nanocomposite for highly efficient co₂ capture," *Journal of CO₂ Utilization*, vol. 34, pp. 543–557, 2019.

- [71] W. Wang, J. Motuzas, X. S. Zhao, and J. C. D. da Costa, "2d/3d amine functionalised sorbents containing graphene silica aerogel and mesoporous silica with improved co₂ sorption," *Separation and Purification Technology*, vol. 222, pp. 381–389, 2019.
- [72] U. Tumuluri, M. Isenberg, C.-S. Tan, and S. S. Chuang, "In situ infrared study of the effect of amine density on the nature of adsorbed co₂ on amine-functionalized solid sorbents," *Langmuir*, vol. 30, no. 25, pp. 7405–7413, 2014.
- [73] C.-H. Huang, W. Klinthong, and C.-S. Tan, "SBA-15 grafted with 3-aminopropyl triethoxysilane in supercritical propane for CO₂ capture," *J. Supercrit. Fluids*, vol. 77, pp. 117–126, may 2013. [Online]. Available: <https://linkinghub.elsevier.com/retrieve/pii/S0896844613000892>
- [74] M. N. A. Tahari and M. A. Yarmo, "Adsorption of co₂ on silica dioxide catalyst impregnated with various alkylamine," in *AIP Conference Proceedings*, vol. 1614, no. 1. American Institute of Physics, 2014, pp. 334–341.
- [75] F. Yan, Y.-S. Liu, and J.-Z. Xiao, "Path Planning in Complex 3D Environments Using a Probabilistic Roadmap Method," *Int. J. Autom. Comput.*, vol. 10, no. 6, pp. 525–533, dec 2013. [Online]. Available: <http://link.springer.com/10.1007/s11633-013-0750-9>
- [76] F. Schler", "'3d path planning for autonomous aerial vehicles in constrained spaces'," Ph.D. dissertation, "2012".
- [77] M. P. Aghababa, "3d path planning for underwater vehicles using five evolutionary optimization algorithms avoiding static and energetic obstacles," *Appl. Ocean Res.*, vol. 38, pp. 48–62, oct 2012. [Online]. Available: <https://linkinghub.elsevier.com/retrieve/pii/S014111871200051X>
- [78] N. K. Yilmaz, C. Evangelinos, P. F. J. Lermusiaux, and N. M. Patrikalakis, "Path planning of autonomous underwater vehicles for adaptive sampling using mixed integer linear programming," *IEEE Journal of Oceanic Engineering*, vol. 33, no. 4, pp. 522–537, 2008.

- [79] H. Choset, S. Hutchinson, K. Lynch, G. Kantor, W. Burgard, L. Kavraki, S. Thrun, and R. Arkin, *Principles of Robot Motion: Theory, Algorithms, and Implementation*, ser. A Bradford book. A Bradford Book, 2005. [Online]. Available: <https://books.google.com.qa/books?id=lr34DwAAQBAJ>
- [80] F. H. Ajeil, I. K. Ibraheem, M. A. Sahib, and A. J. Humaidi, "Multi-objective path planning of an autonomous mobile robot using hybrid PSO-MFB optimization algorithm," *Appl. Soft Comput.*, vol. 89, p. 106076, apr 2020. [Online]. Available: <https://linkinghub.elsevier.com/retrieve/pii/S1568494620300168>
- [81] M. M. AL-Nayar, K. E. Dagher, and E. A. Hadi, "A comparative study for wheeled mobile robot path planning based on modified intelligent algorithms," *The Iraqi Journal for Mechanical and Materials Engineering*, vol. 19, no. 1, pp. 60–74, 2019.
- [82] I. Hassani, I. Maalej, and C. Rekik, "Robot path planning with avoiding obstacles in known environment using free segments and turning points algorithm," *Mathematical Problems in Engineering*, vol. 2018, 2018.
- [83] "Teardown tuesday: Microsoft xbox 360 kinect - news." [Online]. Available: <https://www.allaboutcircuits.com/news/teardown-tuesday-microsofts-xbox-360-kinect/>
- [84] "scanning electron microscope - liberal dictionary." [Online]. Available: <https://www.liberaldictionary.com/scanning-electron-microscope/>
- [85] "Ftir spectroscopy." [Online]. Available: <https://www.sas.upenn.edu/~carrolld/SpecProjectPages/FTIR.html>
- [86] D. R. Cairns, R. P. Witte, D. K. Sparacin, S. M. Sachsman, D. C. Paine, G. P. Crawford, and R. R. Newton, "Strain-dependent electrical resistance of tin-doped indium oxide on polymer substrates," *Applied Physics Letters*, vol. 76, no. 11, pp. 1425–1427, mar 2000. [Online]. Available: <http://aip.scitation.org/doi/10.1063/1.126052>
- [87] M. Vishwas, K. Narasimha Rao, K. V. Arjuna Gowda, and R. P. Chakradhar, "Influence of Sn doping on structural, optical and electrical properties of ZnO

thin films prepared by cost effective sol-gel process," *Spectrochimica Acta - Part A: Molecular and Biomolecular Spectroscopy*, vol. 95, pp. 423–426, sep 2012. [Online]. Available: <https://pubmed.ncbi.nlm.nih.gov/22579328/>

- [88] P. V. Shinde, B. G. Ghule, S. F. Shaikh, N. M. Shinde, S. S. Sangale, V. V. Jadhav, S.-Y. Yoon, K. H. Kim, and R. S. Mane, "Microwave-assisted hierarchical bismuth oxide worm-like nanostructured films as room-temperature hydrogen gas sensors," 2019. [Online]. Available: <https://doi.org/10.1016/j.jallcom.2019.06.182>
- [89] P. V. Shinde, N. M. Shinde, S. F. Shaikh, D. Lee, J. M. Yun, L. J. Woo, A. M. Al-Enizi, R. S. Mane, and K. H. Kim, "Room-temperature synthesis and CO₂-gas sensitivity of bismuth oxide nanosensors," *RSC Advances*, vol. 10, no. 29, pp. 17 217–17 227, may 2020. [Online]. Available: <https://pubs.rsc.org/en/content/articlehtml/2020/ra/d0ra00801j><https://pubs.rsc.org/en/content/articlelanding/2020/ra/d0ra00801j>
- [90] W. R. Abdulmajeed and R. Z. Mansoor, "Implementing kinect sensor for building 3d maps of indoor environments," pp. 975–8887, 2014.